UNIVERSITY OF TARTU

Faculty of Science and Technology

Institute of Technology

Vitor Meira Chaves Barbalho

Iron and nitrogen doped hierarchical porous lignin-derived carbons as oxygen reduction reaction electrocatalysts

Bachelor's Thesis (12 ECTS)

Curriculum Science & Technology

Supervisor(s):

PhD Jaana Lilloja

Prof. Kaido Tammeveski

Tartu 2025

Iron and nitrogen doped hierarchical porous lignin-derived carbons as oxygen reduction reaction electrocatalysts

Abstract

Non-precious metal Fe-N-C electrocatalysts, which can be used as cathode materials for oxygen reduction reaction in an anion-exchange membrane fuel cell were synthesized and investigated by electrochemical and physicochemical methods. The carbon, iron, and nitrogen precursors used to synthesize the electrocatalysts were lignin, iron(II) acetate, and 1,10-phenanthroline, respectively. To obtain the hierarchical porous carbon support, lignin was carbonized using magnesium nitrate hexahydrate as template via high-temperature pyrolysis. Several pyrolysis temperatures (800-1100 °C) were employed to find the optimal carbonization temperature. Iron and nitrogen doping was performed for all carbon materials through flash pyrolysis at 800 °C. The electrocatalytic performance of the prepared Fe-N-C catalyst materials toward the oxygen reduction reaction was studied and compared using the rotating disk electrode method. The physicochemical properties of the catalyst materials were investigated by various analytical methods, namely scanning electron microscopy, scanning transmission electron microscopy, N_2 physisorption, X-ray photoelectron spectroscopy, and Raman spectroscopy.

Keywords

Fe-N-C catalyst, electrocatalysis, hierarchical porous carbon, anion-exchange membrane fuel cell, oxygen reduction reaction, templating, lignin, pyrolysis.

CERCS: P401 Electrochemistry

Institute name: Institute of Chemistry

Research group: Electrocatalysis Group, Chair of Colloid and Environmental Chemistry

Raua ja lämmastikuga dopeeritud ligniinist saadud hierarhilise poorsusega süsinikmaterjalid kui hapniku redutseerumisreaktsiooni elektrokatalüsaatorid

Lühikokkuvõte

Töös valmistati Fe-N-C mitteväärismetallkatalüsaatorid, mida saab kasutada katoodimaterjalina anioonivahetusmembraaniga kütuseelemendis hapniku

redutseerimisreaktsiooni kiirendamiseks, ning neid uuriti elektrokeemiliste ja füüsikalis-keemiliste meetoditega. Elektrokatalüsaatorite sünteesimiseks kasutati süsiniku, raua ja lämmastiku lähteainetena vastavalt ligniini, raud(II)atsetaati ja 1,10-fenantroliini. Hierarhilise poorsusega süsinikkandja saamiseks karboniseeriti ligniin kõrgtemperatuurse pürolüüsi käigus kasutades matriitsina magneesiumnitraat heksahüdraati. Pürolüüsi temperatuuri varieeriti (800–1100 °C) leidmaks sobivaim karboniseerimistemperatuur. Kõigi süsinikmaterjalide puhul viidi läbi raua ja lämmastikuga dopeerimine pürolüüsi teel temperatuuril 800 °C. Valmistatud Fe-N-C katalüsaatormaterjalide elektrokatalüütilist aktiivsust hapniku elektroredutseerimisel uuriti ja võrreldi kasutades pöörleva ketaselektroodi meetodit. Katalüsaatormaterjalide füüsikalis-keemilisi omadusi uuriti erinevate meetoditega, milleks olid skaneeriv elektronmikroskoopia, skaneeriv transmissioon-elektronmikroskoopia, N_2 adsorptsiooni analüüs, röntgenfotoelektronspektroskoopia ja Ramani spektroskoopia.

Võtmesõnad:

Fe-N-C katalüsaator, elektrokatalüüs, hierarhiline poorne süsinik, anioonivahetusmembraaniga kütuseelement, hapniku redutseerumisreaktsioon, matriitsimeetod, ligniin, pürolüüs.

CERCS: P401 Elektrokeemia

TABLE OF CONTENTS

TERMS, ABBREVIATIONS AND NOTATIONS 5

INTRODUCTION 7

1 LITERATURE REVIEW 9

1.1 Anion-exchange membrane fuel cells 9

1.2 Oxygen reduction reaction (ORR) 11

1.3 AEMFC cathode electrocatalysts 12

1.3.1 Metal-Nitrogen-Carbon (M-N-C) electrocatalysts 13

1.3.2 Iron-Nitrogen-Carbon (Fe-N-C) electrocatalysts 16

1.4 Mesoporous carbons 18

2 THE AIMS OF THE THESIS 21

3 EXPERIMENTAL PART 22

3.1 Rotating disk electrode (RDE) method 22

3.2 Preparation of electrocatalysts 24

3.3 Electrochemical measurements 25

3.4 Physicochemical characterization 27

4 RESULTS AND DISCUSSION 29

4.1 Physicochemical characterization of catalysts 29

4.2 Electrochemical characterization of catalysts 35

SUMMARY 40

REFERENCES 41

TERMS, ABBREVIATIONS AND NOTATIONS

AEM	Anion-Exchange Membrane
AEMFC	Anion-Exchange Membrane Fuel Cell
APS	Average Pore Size
CCL	Cathode Catalyst Layer
CL	Catalyst Layer
CV	Cyclic Voltammetry
DAC	Dual-Atom Site Catalyst
DFT	Density Functional Theory
EDX	Energy-Dispersive X-ray Spectroscopy
E_{onset}	Onset Potential
$E_{1/2}$	Half-Wave Potential
Fe-N-C	Iron-Nitrogen-Carbon
GC	Glassy Carbon
HAADF	High-Angle Annular Dark-Field
HPC	Hierarchical Porous Carbon
j_d	Diffusion-Limited Current Density
K-L	Koutecký-Levich
MC	Mesoporous Carbon
MEA	Membrane Electrode Assembly
M-N-C	Metal-Nitrogen-Carbon
n	Number of Electrons Transferred per O_2 Molecule
NPs	Nanoparticles
OMC	Ordered Mesoporous Carbon
ORR	Oxygen Reduction Reaction
PEM	Proton-Exchange Membrane
PEMFC	Proton-Exchange Membrane Fuel Cell
PGM	Platinum Group Metal
PSD	Pore Size Distribution
RDE	Rotating Disk Electrode
SAC	Single-Atom Site Catalyst
SCE	Saturated Calomel Electrode
SEM-EDX	Scanning Electron Microscopy with Energy-Dispersive X-ray Analysis
SD	Site Density

SSA	Specific Surface Area
STEM	Scanning Transmission Electron Microscopy
TPB	Triple-Phase Boundary
XAS	X-ray Absorption Spectroscopy
XPS	X-ray Photoelectron Spectroscopy

INTRODUCTION

Since the industrial revolution, human civilization has become increasingly dependent on the use of fossil fuels, such as coal, petroleum and natural gas, for its energy needs. This relatively cheap and abundant energy source has been required for industrial societies to thrive. Nowadays, the main uses of the energy provided by fossil fuels are heating, transportation and electricity generation. The rapid increase in global population with subsequent exponential increase in energy consumption has led to concerns that this once cheap and plentiful energy source will become steadily more scarce and expensive. Additionally, the huge amount of fossil fuels that are used daily around the world has led to concerns among scientists and the general public about the ecological impacts on the Earth's environment caused by the substantial carbon dioxide emissions generated from the combustion of fossil fuels (Hossen et al., 2023).

Alternative energy generation technologies, together with alternative energy sources, have increasingly been explored as a replacement for fossil fuels as an energy source. One type of alternative technology device, among many others, that can be used as replacement, is the fuel cell (Nazir et al., 2020). Fuel cells are able to directly generate electrical energy from the chemical energy of fuels. A commonly used fuel is hydrogen gas (H_2) that reacts with an oxidant, e.g. oxygen gas (O_2) present in the atmosphere, forming (by)products, e.g. water (H_2O), and generating electricity in the process.

Proton-exchange membrane fuel cells (PEMFC) are already well-established and commercially available. While PEMFCs can convert chemical energy of fuels into electricity with high efficiency, it has several drawbacks. The most significant one is the use of platinum or platinum-group metal (PGM)-based electrocatalyst materials on both electrodes, cathode and anode, to achieve the desired performance needed for its commercial applications. Pt and PGMs are scarce and expensive raw materials that make PEMFCs significantly less economically attractive than otherwise if they were not needed (Wang et al., 2011) (Hren et al., 2021).

A similar but competing fuel cell technology to PEMFCs is the anion-exchange membrane fuel cell (AEMFC). Contrary to the PEMFC, AEMFC cathodes can use PGM-free electrocatalysts while delivering similar performance to ones based on PGM materials. Among PGM-free materials, the metal-nitrogen-carbon (M-N-C, M = Fe, Co, Mn, etc.) electrocatalysts have the most potential to replace the Pt-based ones, and have been the focus of significant research lately. The M-N-C catalysts exhibit outstanding electrocatalytic performance, high stability, low price, and abundant reserves worldwide (Zhang et al., 2022).

This thesis investigates the performance of mesoporous Fe-N-C electrocatalysts that can be used in AEMFC cathodes to the catalyze oxygen reduction reaction. They are synthesized via pyrolysis of iron, nitrogen, and carbon precursors at high temperatures. The carbon source used for the production of the mesoporous carbon support was lignin (Lignova™, Fibenol OÜ) that was combined with magnesium nitrate as a template. The iron source was iron(II) acetate and the nitrogen source was 1,10-phenanthroline. All these materials are relatively inexpensive and readily available, ideal for the economic feasibility and sustainability of AEMFCs.

1 LITERATURE REVIEW

1.1 Anion-exchange membrane fuel cells

Fuel cells are electrochemical devices that directly convert chemical energy of fuels, such as hydrogen, into electrical energy. The efficiency of fuel cells can reach as high as approximately 80% when used for the co-generation of electricity and heat, and about 60% when used for electricity only (Wang et al., 2011), which is generally higher than that of the internal combustion engines (Fu et al., 2023) (Braga et al., 2014).

Fuel cells are classified according to the electrolyte employed (Wang et al., 2011). Among others, polymer electrolyte membrane fuel cells and solid oxide fuel cells have been the most researched. Polymer electrolyte membrane fuel cells can be classified further into proton-exchange membrane fuel cells (PEMFCs) and anion-exchange membrane fuel cells (AEMFCs) (**Figure 1**).

AEMFCs are similar in technology to PEMFCs. In AEMFCs, the solid membrane is an alkaline anion-exchange membrane (AEM) instead of an acidic proton-exchange membrane (PEM) used in PEMFCs. In an AEM, the hydroxide (OH^-) anion is transported from the cathode to the anode, opposite to the proton (H^+) conduction direction in a PEM (**Figure 1**). The AEM in AEMFCs is a solid polymer electrolyte, which contain positively charged cationic groups bounded to, or part of, the polymer backbone. Both PEMFC and AEMFC produce only water as a byproduct when pure hydrogen is used as fuel. However, in contrast to PEMFC technology, in an AEMFC water is generated at the anode (twice as much as in a PEMFC, per electron), while at same time water is a reactant at the cathode in AEMFCs (Dekel, 2018).

Generally, PEMFCs exhibit higher performance than AEMFCs and are already commercially available. However, recent advances in the AEMFC technology have closed the performance gap considerably. In addition, AEMFCs do not present several drawbacks that are preventing PEMFC technology to progress further, such as the strict requirement for platinum catalyst materials in the cathode (Gottesfeld et al., 2018) (Sarapuu et al., 2023). While the less corrosive alkaline environment in the AEMFC allows the use of inexpensive non-noble metals and non-metal catalysts, the acidic conditions in the PEMFCs is detrimental even for noble metal-based catalysts, such as Pt, which leads to durability issues on the latter and makes the choice of materials for PEMFC more restrictive and difficult. Also, catalyst degradation by hydrogen peroxide (H_2O_2) is more severe in acidic conditions than alkaline. Additionally, unlike PEMs, AEMs can be synthesized without the use of fluorinated compounds, which are expensive and toxic (Hossen et al., 2023).

The AEM is a principal component of the AEMFCs. It should have high OH^- anion conductivity, exhibit no electronic conductivity, curb fuel crossover, and retain its physico-mechanical properties in its hydrated state (Das et al., 2022). Among several reasons for the deterioration of performance in AEMFCs, the main reason is probably the chemical degradation caused by the attack of the hydroxide ion (OH^-) on the anion conducting polymers (ionomers), which occurs under the alkaline environment of the AEMFC. This degradation leads to a reduction in AEM anion conductivity, which increases the cell internal resistance and reduces the cell durability. The chemical degradation of the AEMs and its negative effect on the cell performance is one of the major challenges faced by AEMFCs technology, which hinders its progress and commercial availability (Dekel, 2018).

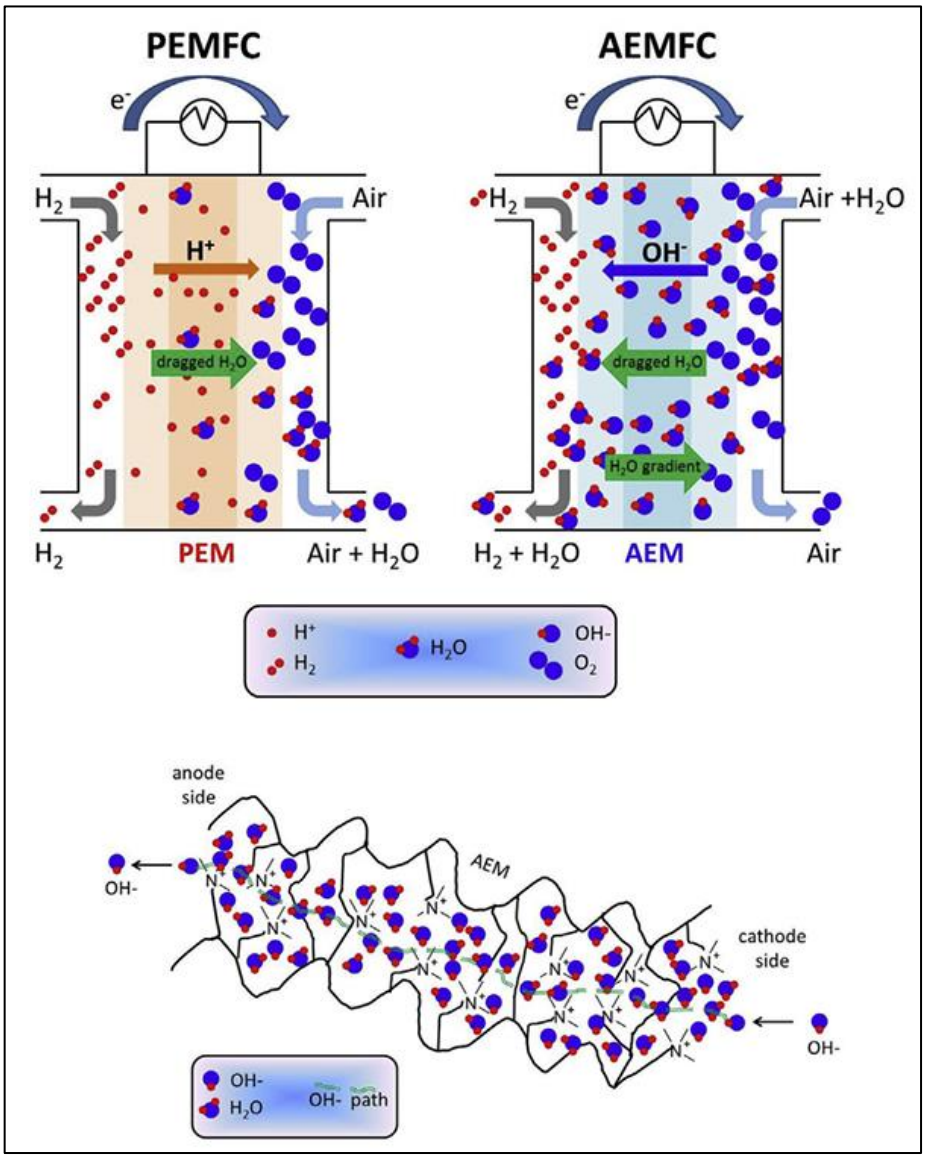

Figure 1. Schematic of an AEMFC as compared to a PEMFC (top scheme), and of an AEM based on a quaternary ammonium pendant functional group (bottom scheme) (Dekel, 2018).

The core of the AEMFC is the membrane-electrode assembly (MEA). The MEA is a layered structure consisting of the anion-exchange membrane (AEM) sandwiched between two catalyst layers and two gas diffusion layers for the anode and cathode, respectively. The catalyst layer (CL) is commonly obtained from a catalyst ink, which is usually composed of an electrocatalyst material, an ionomer and a solvent. The solvent is normally evaporated during the fabrication process. The chemicals and preparation method of the CL will determine its structure, properties and electrocatalytic performance. Once the MEA is assembled, it can be operated on a fuel cell test bench to have its performance evaluated by electrochemical measurements, such as polarization curve or cyclic voltammetry (Turtayeva et al., 2024).

1.2 Oxygen reduction reaction (ORR)

The oxygen reduction reaction refers to the electrochemical process where oxygen (O_2), in the presence of water, is reduced (i.e. gain electrons) to produce hydroxide ions (OH^-). In AEMFCs, this reaction occurs at the cathode catalyst layer (CCL) and is essential for the fuel cell to generate electricity. The ORR is a sluggish reaction and a rate-limiting process in fuel cells. The ORR is more favorable with a faster electrochemical kinetics in alkaline than acidic conditions and hence the alkaline media in AEMFCs allows the use of lower catalyst loading than PEMFCs (Hossen et al., 2023).

In alkaline media, the ORR may either follow a direct 4-electron pathway, 2-electron pathway or a two-step 2-electron (2+2) pathway as shown below (Sljukic et al., 2005):

Direct **4-electron** ORR pathway:

$$O_2 + 2\ H_2O + 4\ e^- \rightarrow 4\ OH^- \quad (1)$$

2-electron ORR pathway:

$$O_2 + H_2O + 2\ e^- \rightarrow HO_2^- + OH^- \quad (2)$$

Followed by electroreduction of the hydroperoxide anion during the **2+2e⁻** pathway:

$$HO_2^- + H_2O + 2\ e^- \rightarrow 3\ OH^- \quad (3)$$

The **anode** reaction in a fuel cell in alkaline media occurs as follows:

$$2\ H_2 + 4\ OH^- \rightarrow 4\ H_2O + 4\ e^- \quad (4)$$

The **overall** reaction of the fuel cell is:

$$O_2 + 2\ H_2 \rightarrow 2\ H_2O \quad (5)$$

The percentage yield of peroxide formation should be as low as possible for excellent ORR electrocatalysis. The peroxide produced by the 2-electron pathway (Eq. 2) is potentially damaging the fuel cell catalysts and membranes, and reduces the fuel cell efficiency. As a result, the 4-electron pathway is the desired one for ORR. Since the ORR has a slow reaction rate because of the high energy required to break the O-O bond, the search and optimization of high-performance cathode catalysts is of great importance (Hossen et al., 2023). Furthermore, in addition to good electrocatalytic ORR activity, it is crucial that catalyst materials possess long-term stability, especially in fuel cell operating conditions (Lilloja et al., 2024).

The triple-phase boundary (TPB) is the interface where the oxygen (gas), ion-transportation medium (water present in the ionomer − liquid), and catalyst particles (solid) come into contact during the catalytic reaction process. The TPB has major impact on the rate of ion, electron, and mass transport in the fuel cell. Therefore, understanding the TPBs is essential to optimize the ORR and, consequently, the overall performance (Cao et al., 2021).

The efficiency of the ORR is heavily dependent on the quality and quantity of effective TPB sites. If the catalyst layer is designed such that there are many TPB sites where the catalyst is well-connected to both the ionomer and the gas phase, the reaction can proceed more efficiently. For instance, excessive ionomer will reduce the porosity of catalyst layer and hinder the transfer pathway for water and oxygen, increasing the mass-transfer resistance. On the other hand, insufficient ionomer can result in poor coverage and a small amount of TPB sites being formed, leading to lower electrocatalytic activity. Thus, for any specific AEMFC, the appropriate ratio of ionomer and catalyst material needs to be investigated to balance mass-transfer resistance and TPB formation, and achieve higher performance (Zhang et al., 2021) (Chae et al., 2024) (Miyazaki, 2014).

1.3 AEMFC cathode electrocatalysts

Until recently, AEMFCs have required a relatively high loading of PGM-based catalysts at both the anode and cathode electrodes to achieve a competitive fuel cell performance relative to PEMFCs (Firouzjaie & Mustain, 2020). The main reason for this is that PGM-based catalysts, such as carbon-supported platinum nanoparticles (Pt/C), still have one of the highest ORR activity in alkaline media (Zhang et al., 2021). However, the high price of Pt and other PGMs significantly increases the cost of AEMFCs, which is a major economic barrier to their widespread adoption (Sarapuu et al., 2023). In addition, another challenge is that Pt

nanoparticles are prone to leaching from the carbon support, and likely to reduce the overall performance of the fuel cell (Collins et al., 2023).

The long-established catalysts used for ORR at the cathode are PGM-based ones. Pt/C is commonly used in research for benchmarking and comparing it with alternative emerging technologies. They are suitable to be used in both acidic (e.g. PEMFCs) and alkaline media (Hren et al., 2021). The reasons that carbon support is best suited for this purpose it is because it provides a large surface area for the active metals to be well-dispersed, forms pores for gas and water transport, and also serves as a good electronic conductor (Chae et al., 2024). Besides Pt/C, many Pt-alloy catalysts with reduced Pt content, have also been used. These catalysts are typically combined with a secondary non-PGM, such as transition metals, to obtain a lower cost but with a comparable electrocatalytic performance material. They can be alloyed together or have a core-shell structure. Among others, PtRu, PtNi, PtCu, and PtCo catalysts are some examples that have been reported in the scientific literature (Zhang et al., 2021). The inherent non-corrosive environment of AEMFCs allows the use of electrocatalysts with less noble metal content for the ORR (Hren et al., 2021) (Adabi et al., 2023).

Metal-nitrogen-carbon (M-N-C, where M = Fe, Co, Mn, etc.) electrocatalysts are the most promising materials to replace Pt-based catalysts due to the low cost and abundant availability of raw materials, outstanding ORR catalytic performance, and high stability. The metal ions act as main catalytic centers, while the heteroatoms enhance electrocatalytic activity. Doped nitrogen promotes the formation of active N-C sites. However, M-N-C catalysts face challenges, such as chemical degradation and difficulties in achieving a suitable porosity and sufficient accessible active sites (Zhang et al., 2022). M-N-C catalysts will be discussed in greater detail in subsequent sections.

1.3.1 Metal-Nitrogen-Carbon (M-N-C) electrocatalysts

M-N-C catalysts are a class of non-precious metal electrocatalysts characterized by transition metals atomically dispersed and coordinated with nitrogen atoms within a carbon matrix. Carbon makes up most of the material by atomic percentage (at.%). The porous carbon matrix are commonly obtained, among other possible sources, from carbon black (e.g. Vulcan XC-72), graphene, carbon nanotubes, mesoporous carbons, carbide-derived carbon, or biomass-derived carbon (Sarapuu et al., 2023). Carbon is generally used as a support material because of its good mechanical strength, chemical stability, high electrical conductivity, and high specific surface area (Hossen et al., 2023). The chosen carbon precursor will partly

determine the final catalyst properties, structure and performance. Combining two or more carbon materials, like composites, as support can lead to even more advantageous catalyst structures (Lilloja et al., 2024).

The synthesis of M–N–C catalysts typically involves several steps, each influencing the chemistry and morphology of the final electrocatalyst. They can be synthesized from a mixture of carbon and precursors rich in nitrogen and the desired transition metal that is subjected to high-temperature treatment between 600 and 1100 °C in an inert atmosphere (pyrolysis). The resulting materials can display a large degree of porosity, high surface area, and high graphitization. The graphitic carbon network obtained from pyrolysis commonly possesses abundant nitrogen and transition metal defects (Artyushkova et al., 2019). However, the pyrolysis process is difficult to control in regard to achieving the desired pore sizes and surface compositions in the catalyst support (Zhang et al., 2021). A great variety of nitrogen sources can be used for doping, and they can be grouped into the following precursor types: small organic molecules, polymers, reactive gases such as ammonia (NH_3), and nitrogen-containing metal complexes. Each precursor can give a different contribution to the properties of the final catalyst (Chen et al., 2011). Nitrogen doping can result in pyridinic, pyrrolic, or graphitic nitrogen within the carbon matrix (**Figure 2**) (Inagaki et al., 2018).

M-N-C catalysts can be single-atom site catalysts (SACs) or dual-atom site catalysts (DACs). The active sites of the latter contain pairs of metal atoms located near or adjacent to each other and can offer an improved electrocatalytic activity over SACs due to the formation of unique electronic structures (Sarapuu et al., 2023). The transition metals commonly used, for both SACs and DACs, include iron (Fe), cobalt (Co), manganese (Mn), and less frequently, nickel (Ni), copper (Cu), and zinc (Zn). When simple transition metals salts are used as precursors, acetates, nitrates and chlorides are typically employed (Sarapuu et al., 2023). The required metal content can be rather low, even less than 1 wt.% (Lilloja et al., 2024). The co-existence of metal nanoparticles (NPs) and M−N_x sites can enhance the ORR activity. For instance, Fe-N_x sites and iron nanoparticles jointly contribute toward O_2 adsorption and also O–O bond cleavage (Ahmed et al., 2024). Some examples of metal NPs and M−N_x coupled catalytic sites are: Fe-N_x sites coupled with Fe NPs, Co-N_x sites coupled with Co NPs, Fe-N_x sites coupled with Ni NPs, and Fe-N_x sites coupled with Fe_3C NPs (Lu et al., 2023).

Apart from theoretical modelling such as density functional theory (DFT) calculations, the chemistry of M-N-C catalysts can be investigated using spectroscopic techniques, including Mössbauer, X-ray photoelectron spectroscopy (XPS), and X-ray absorption spectroscopy (XAS). XPS is an analytical method capable of measuring the surface elemental concentration

of M–N–C catalysts within the top 5–11 nm, directly correlating with their electrochemical performance. The development of M–N–C catalysts for ORR have been advanced by research based on the correlation between the surface composition and ORR performance (Artyushkova et al., 2019). The good electrocatalytic performance of the M−N−C materials predominantly arise from the presence of transition metal atoms coordinated to nitrogen moieties (M-N_x) (Lilloja et al., 2024). Specifically, the catalyst should have higher quantities of atomically dispersed M-N_x centers, especially coordinated with pyridinic nitrogen or as porphyrin-like moieties, along with minimal amount of hydrogenated and protonated edge sites (Artyushkova et al., 2019). Studies indicates that M−N_4 sites in the M−N−C catalysts are the most active for ORR. (Lu et al., 2023).

Besides proper chemical composition, such as active N-moieties and M-N_x sites, the M-N-C type catalysts also need a suitable structure, namely, high mesoporosity (Lilloja, Mooste, et al., 2021). A mesoporous structure in the catalyst material is considered beneficial because micropores (< 2 nm) and active sites embedded within them could be blocked by the ionomer and be inaccessible to O_2 molecules. To obtain a high performance final catalyst, not only the chosen support material should be uniformly structured with a high specific surface area, but it is also important the active sites have high accessibility for O_2 molecules (Lilloja et al., 2024).

The turnover frequency (TOF) value, which is defined as the number of chemical conversions of reactant molecules per unit time per catalytic site, is a fundamental parameter to characterize the intrinsic catalytic activity of atomically dispersed centers. Another important parameter is the site density (SD), which is the number of active sites accessible to reagents. For improvement of the electrocatalytic activity, it is desirable that the SD be as high as possible. This is achieved by optimizing the morphology of carbon matrix, such as increasing the specific surface area and obtaining a favorable porous structure (Sarapuu et al., 2023). A significant challenge in the characterization of electrocatalysts is the absence of straightforward experimental methods to assess site density. During the preparation of electrocatalysts by high-temperature pyrolysis, multiple types of ORR-active sites are formed concurrently. Moreover, even in materials with only M-N_x sites, the SD cannot be determined from the total metal content in the electrocatalyst, as some M-N_x sites are embedded within the carbon matrix and not accessible to reagents (Sarapuu et al., 2023).

Spectroscopic techniques, including X-ray absorption spectroscopy, ^{57}Fe Mössbauer spectroscopy, and X-ray photoelectron spectroscopy, cannot differentiate between accessible and inaccessible M-N_x sites. However, by applying techniques which use probe molecules or ions like CO, NO, or CN^-, which selectively bind to the accessible metal sites, it is possible to

quantify them. The ratio of the number of M-N_x sites that are electrochemically accessible to the number of all M-N_x moieties is referred to as "site utilization factor" (Sarapuu et al., 2023).

Despite the excellent intrinsic activity of M-N-C catalysts, their overall electrocatalytic performance is moderate, limiting their practical application. Achieving a site density similar to a Pt/C catalyst with an atomically dispersed M-N-C catalyst is highly challenging. By design, transition metals must be isolated from one another in M-N_x sites, which are themselves separated within the carbon lattice. Merely increasing the metal content in the catalyst precursor does not necessarily result in a higher amount of effective active sites, as the inaccessible active sites might increase relatively more than the accessible ones. Another challenge is that metal atoms tend to aggregate into particles during high-temperature pyrolysis (Cai et al., 2022) (D. Wang et al., 2022).

At present, the ORR electrocatalytic activity of M–N–C catalysts is close to or even outperforms that of the PGM-based catalysts in alkaline media (Han & Liu, 2024). However, this high ORR activity is obtained while testing the electrocatalysts using the rotating disk electrode (RDE) setup. Inconsistencies between the RDE and AEMFC performance during testing, due to the influence of ionomer and ion exchange membrane, are usually present. Satisfactory AEMFC performance and long-term stability using those catalysts in contact with polymer electrolytes have not been achieved yet (Zhang et al., 2021) (Gottesfeld et al., 2018).

1.3.2 Iron-Nitrogen-Carbon (Fe-N-C) electrocatalysts

Fe-N-C catalysts are a subtype of M-N-C SACs in which the atomically dispersed transition metal within the nitrogen-doped carbon support is iron. Studies indicate that Fe-N-C catalysts possess outstanding performance in alkaline media and great potential to replace PGM-based catalysts in AEMFC cathodes (Sarapuu et al., 2023). The alkaline environment in anion exchange membrane fuel cells (AEMFCs) is beneficial for Fe–N–C catalysts, enhancing both their activity and stability. For instance, catalyst deactivation due to oxidative H_2O_2 attack is considerably less severe in alkaline media than in acidic conditions (Hossen et al., 2023).

Among PGM-free cathodes, the best AEMFC performance has been obtained with iron-based SAC (Adabi, Shakouri, et al., 2021) (Sarapuu et al., 2023). Fe–N–C catalysts with Fe being present only or mainly as atomically-dispersed Fe-N_4 moieties have shown one of the highest ORR mass-activity in RDE tests (Adabi, Santori, et al., 2021). On the other hand, the measurement protocols for evaluating Fe–N–C catalysts as AEMFC cathodes are not yet fully developed, making comparisons between research groups more difficult (Teppor et al., 2024).

A common method for achieving atomic dispersion of transition metals involves the use of metal-organic frameworks, particularly zeolitic imidazolate frameworks, to create high-performing single-atom catalysts (SACs) for ORR. Many iron-based SACs can be synthesized using iron(II) acetate and 1,10-phenanthroline as precursors. 1,10-phenanthroline coordinates with transition metal ions, forming complexes with M-N_x speciation that promote the atomic dispersion of transition metal in the final catalyst material (Lilloja et al., 2024).

Similarly to other M-N-C catalysts, the carbon matrix of Fe-N-C catalysts obtained by doping and pyrolysis typically contain the following defects and functional groups, which may vary depending on the pyrolysis parameters and precursors used (Artyushkova et al., 2019).

- Carbon-oxygen defects at the edges such as surface oxides;
- A collection of nitrogen defects located both at the edges and in-plane graphene matrices. The edges of the carbonaceous material may be terminated with imine, amine, pyridinic nitrogen, hydrogenated nitrogen, including pyrrolic and hydrogenated pyridine, and also quaternary nitrogen (see **Figure 2**).
- Within the plane of carbonaceous material, N–O groups, graphitic nitrogen and nitrogen coordinated with iron in various FeN_x–C configurations, where x ranges from 1 to 4, may be present (see **Figure 2**). The preferential chemical state of iron is iron coordinated with nitrogen, although residual iron-rich phases, such as iron oxide, iron carbide, and metallic iron nanoparticles, may also be present.

Fe-N-C catalysts are characterized by low bulk density (high porosity) and presumed low density of ORR-active sites. Consequently, current PGM-free catalyst layers (CLs) are significantly thicker than those using PGM catalysts. Therefore, to achieve reasonable ORR activity in AEMFC operating conditions, the cathode catalyst loading must be increased. Compared to conventional PGM electrodes, PGM-free electrodes typically are approximately ten times thicker (5 μm for PGM-based vs. 50–100 μm for PGM-free cathodes). This increased thickness poses challenges for designing a CL which is suited to the mass transport and conductivity requirements of a fuel cell. When the CL is thicker, oxygen, ions, and electrons travel longer distances, leading to a higher overpotential and ohmic losses (Serov et al., 2018).

Nevertheless, a study by Adabi et al. demonstrated that single-atom-dominated Fe-N-C catalyst layers can have excellent performance and durability in an H_2/O_2 AEMFC, achieving a peak power density of 1.8 W cm^{-2}, comparable to an AEMFC using a Pt/C cathode, and maintaining stable operation for over 100 h. To construct the H_2/O_2 AEMFC, the Fe-N-C cathode was combined with a low-loading PtRu/C anode catalyst (Adabi, Santori, et al., 2021).

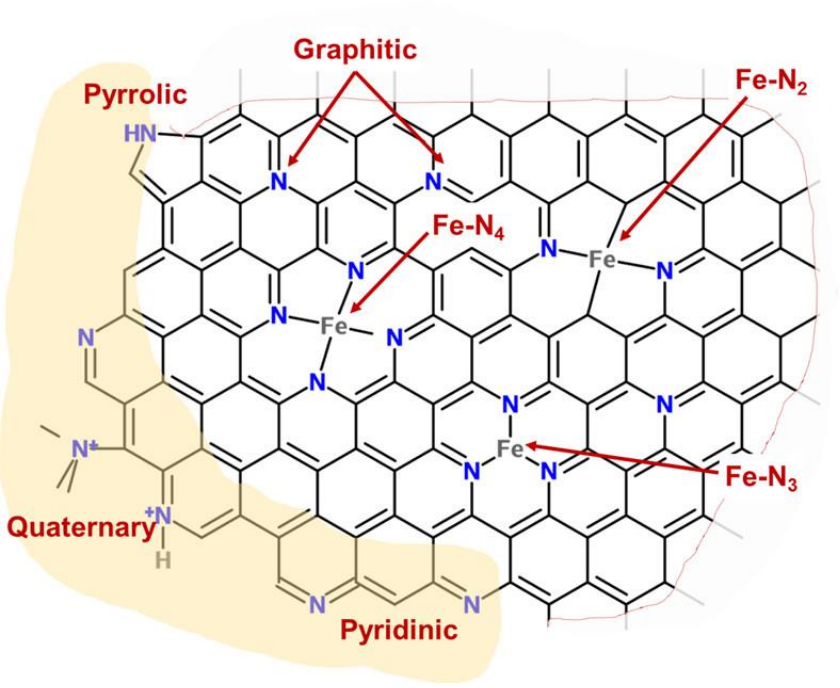

Figure 2. Nitrogen and Fe-N_x groups present in Fe-N-C materials (Artyushkova et al., 2015).

1.4 Mesoporous carbons

Mesoporous carbons (MCs) are carbon materials with pore sizes within the 2-50 nm range. According to the IUPAC definition, mesoporous materials have intermediate size range between microporous materials, which are the ones having pores smaller than 2 nm in diameter, and macroporous ones, which have pores larger than 50 nm in diameter (ROUQUEROL et al., 1994). It is important to note that this classification is an artificial one, and materials can have a pore size distribution that fall inside two or even all three ranges. In the case of carbon materials, these are called hierarchical porous carbons (Fu et al., 2011). Mesoporous carbons are exceptional and versatile materials which have multiple technological applications (Rahman et al., 2021). Some key properties or advantages of mesoporous carbons include (Mehdipour-Ataei & Aram, 2023): high specific surface area; large pore volume; controllable porous structure; good electronic conductivity; chemical and thermal stability; low cost of synthesis.

MCs can be of ordered or disordered porous structure. The former is called ordered mesoporous carbon (OMC). MCs and OMCs are similar in terms of pore sizes, with OMC having a well-ordered and uniform assembly and network of mesopores. MC is unique from an electrochemical viewpoint, as the pore sizes are sufficiently small for the material to have a high specific surface area, but also appropriately large for the diffusion of reactant molecules and electrolyte ions. Conversely, microporous carbons have too small pores for the transport of electrolytes and reactants, while macroporous ones have significantly lower specific surface

area. This property makes mesoporous carbons ideal supports for ORR electrocatalysts in AEMFCs, where the cathode catalyst layer requires efficient oxygen diffusion and also water management (Collins et al., 2023). Hierarchical porous carbons (HPCs) which contain interlinked macro- and meso-porous structures exhibit enhanced diffusion and mass transfer compared to traditional mesoporous carbons. This is particularly advantageous for ORR electrocatalysts, which can use HPCs as catalyst support, such as Pt/C and M-N-C catalysts (Collins et al., 2023).

The synthesis methods for mesoporous carbon materials can be classified into template methods and template-free methods (Xu et al., 2022). Based on the template agent's nature and role, the template methods can be categorized into hard-template, soft-template, or dual-template methods. Template-free methods can be classified into solvothermal methods, sol-gel methods, and pyrolysis methods (Zhou et al., 2025). The template method is a key synthesis approach used for preparing mesoporous carbon materials. In this technique, a template agent forms pore structures through chemical interactions with the carbon precursor, which is followed by template removal to yield the desired material. The template method's strength is its controllability over pore size, structure, and morphology. The templating methods have become important routes for achieving high-performance mesoporous carbon materials due to its outstanding tunability (Zhou et al., 2025).

The hard template method employs solid materials such as mesoporous silica as templates. The carbon precursor is introduced into the template's pores or it surrounds the hard template particles, followed by carbonization and subsequent chemical etching to remove the template, yielding a material with a mesoporous structure, which is inverse of its template. For etching, acidic or alkaline conditions can be used. Materials synthesized this way generally exhibit uniform pore sizes and highly ordered pore structures, such as OMC. However, template removal can attack and change the material properties and mesoporous structure, and may also pose environmental hazards, e.g. when HF is employed to remove silica template (Zhou et al., 2025) (Collins et al., 2023).

The soft template method uses the self-assembly of surfactants or block copolymers in solution to form flexible templates. The carbon precursor interacts with the template agent to form the desired structure, followed by heat-treatment to carbonize the material and remove the template, resulting in the mesoporous material. The pore order and structural stability of these materials are typically lower compared to those made by the hard template method (Zhou et al., 2025).

The dual-template method, which combines the benefits of hard and soft template methods, can be used to synthesize materials with hierarchical pore structures. In this approach, the hard template provides support for the macroscopic structure, while the soft template directs the formation of microscopic pores, enabling simultaneous control of macro- and micro-structure. This method can produce materials with both high order and hierarchical structure, but it is more complex and expensive than the previous two approaches (Zhou et al., 2025).

Another approach for achieving hierarchical porosity in carbon materials is through ionothermal synthesis. A carbon-rich precursor, such as a biomass-derived material, is mixed with a low-melting point salt (e.g. a Mg or Zn salt), which serves as template. The mixture is then pyrolyzed and cooled to ambient temperature. A porous carbon nanostructure is achieved after removing the in-situ formed non-carbon nanoparticles (e.g. magnesium oxide (MgO) in the case of $Mg(NO_3)_2$ via acid treatment. The resulting porosity is largely determined by the interaction between the chosen carbon precursor and molten salt. In addition, the choice of salt can significantly affect the nanostructure, and, to a certain limit, adjusting the salt-to-carbon precursor ratio can alter the resulting carbon material structure (Kisand et al., 2025).

The aforementioned approach is used to synthesize hierarchical porous carbon with abundant mesopores in this work. The carbon precursor was lignin (Lignova™ – Fibenol OÜ) and the low-melting point salt was magnesium nitrate hexahydrate ($Mg(NO_3)_2 \cdot 6H_2O$). They were mixed in a 1:2 mass ratio, respectively. Lignin is an abundant component in plant biomass and a waste product of the paper industry. Due to its high carbon content, lignin can be used as a precursor for the preparation of carbon materials by pyrolysis (Sajjad et al., 2024).

2 THE AIMS OF THE THESIS

The aim of the thesis is to develop non-precious metal catalyst materials suitable for oxygen reduction reaction electrocatalysis.

- Prepare hierarchical porous carbon materials with abundant mesopores from lignin using templating approach and varied carbonization temperature (800-1100 °C).
- Prepare iron- and nitrogen-doped electrocatalysts based on lignin-derived carbons using pyrolysis.
- Investigate the effect of carbonization temperature on the physicochemical properties of the catalyst materials.
- Study the oxygen reduction reaction activity and electrochemical stability of the prepared Fe-N-C electrocatalysts.
- Investigate the effect of carbonization temperature on the electrocatalytic ORR behavior.

3 EXPERIMENTAL PART

3.1 Rotating disk electrode (RDE) method

The ORR electrocatalytic activity of the catalyst materials is normally assessed using electroanalytical techniques, such as cyclic voltammetry and linear sweep voltammetry, with the rotating disk electrode (RDE) or rotating ring-disk electrode methods. To evaluate the electrocatalytic activity of distinct electrode materials, one can compare the current density at a fixed overpotential or measure the overpotential at a fixed current density. An effective electrocatalyst should exhibit high current density at a low overpotential. The electroanalytical techniques mentioned above possess several advantages and are important to study the structure-activity relationship and limiting factors of catalyst materials. The main advantages of RDE method are as follows (Collins et al., 2023) (Hossen et al., 2023):

- Standard protocol;
- A small amount of catalyst required;
- A well-established methodology available to determine the kinetic parameters.

However, the experimental conditions in these techniques normally differ from the practical environment of the fuel cells in several aspects, such as (Hossen et al., 2023):

- Thinner layer of catalyst in RDE;
- Rotation of working electrode;
- Small electrode area;
- Current density at different range;
- Glassy carbon disk is used as a substrate instead of a gas diffusion layer;
- Differences in gas flow patterns.

Several other alternative techniques, which are expected to improve the understanding of the activity, stability and other properties of catalyst materials, have been proposed, such as the conventional gas-diffusion electrode method (Hossen et al., 2023).

For linear sweep voltammetry the RDE experiments in O_2 saturated electrolyte solution in a three-electrode electrochemical cell are conducted and the RDE polarization curves are recorded at each electrode rotation rate. RDE polarization curves are showcased as current density (mA cm^{-2}) on the y-axis against potential (V) on the x-axis. The current density is obtained from the measured current divided by the geometric area of the working electrode, after being corrected for the background currents measured in Ar-saturated electrolyte. The data

is analyzed using the Koutecký-Levich (K-L) equation and the K-L plots are constructed (Bard et al., 2022):

$$\frac{1}{j} = \frac{1}{j_{\mathrm{k}}} + \frac{1}{j_{\mathrm{d}}} = -\frac{1}{nFk\,C^{b}_{\mathrm{O_2}}} - \frac{1}{0.62\,nF\,D^{2/3}_{\mathrm{O_2}}\,v^{-1/6}\,C^{b}_{\mathrm{O_2}}\,\omega^{1/2}} \tag{6}$$

where:

- j is the measured current density,
- j_k and j_d are the kinetic and diffusion-limited current densities, respectively,
- ω is the electrode rotation rate (rad s^{-1}),
- n is the number of electrons transferred per O_2 molecule,
- k is the electrochemical rate constant for O_2 reduction (cm s^{-1}),
- F is the Faraday constant (96,485 C mol^{-1}),
- C_{O2}^{b} is the concentration of oxygen in bulk (1.2×10^{-6} mol cm^{-3}),
- D_{O2} is the diffusion coefficient of oxygen (1.9×10^{-5} cm^2 s^{-1})
- and ν is the kinematic viscosity of the electrolyte solution (0.01 cm^2 s^{-1}).

The Koutecký-Levich equation is an important tool that is generally used for the correction of mass transport effects in RDE testing to obtain the ORR kinetic current densities, and the equation is obtained from two fundamental assumptions (Xu et al., 2017):

- A linear diffusion model of reactants,
- The electrochemical reaction follows first-order reaction kinetics.

However, it is important to note that these assumptions may not always hold true during RDE testing, where for nanostructured catalysts, the linear diffusion assumption may not be valid as oxygen supply might be affected by processes other than diffusion in the electrolyte. Similarly, the ionomer within the catalyst material can influence the reactant diffusion (Xu et al., 2017). For the Koutecký-Levich plots, the inverse of current density, $1/j$ (mA^{-1} cm^2), is plotted against the inverse of the square root of rotation rate, $1/\omega^{1/2}$ ($rad^{-1/2}$ $s^{1/2}$), at several potentials. A linear relationship is obtained, in which the slope of the K-L plot is $1/B$, and the intercept of the extrapolated K-L- lines is $1/j_k$. The kinetic current density (j_k) can be calculated from the intercept value. The higher j_k, the more active the electrocatalyst (Q. Wang et al., 2022). The number of electrons transferred (n) per O_2 molecule can be calculated from the slope of the K-L plot ($1/B$). This allows one to evaluate whether the catalyst promotes the 4-electron ORR pathway (n = 4; Eq. 1) or the 2-electron pathway (n = 2; Eq. 2).

3.2 Preparation of electrocatalysts

The electrocatalyst material under study in this thesis is a non-precious metal Fe-N-C catalyst. Four similar materials were prepared Fe-N-C800, Fe-N-C900, Fe-N-C1000 and Fe-N-C1100. As detailed below, the end numbers represent the carbonization temperature employed to obtain mesoporous carbon support. All the catalysts were prepared from three precursors:

(i) Lignin (Lignova™ – Fibenol OÜ),

(ii) Iron(II) Acetate (95%, Aldrich),

(iii) 1,10-Phenanthroline (99+%, Acros Organics).

These precursors are the carbon, iron and nitrogen sources, respectively, for the preparation of electrocatalysts. The synthesis protocol can be separated into two stages: the making of carbon material and the doping of the carbon material to obtain the Fe-N-C catalyst.

The first step consisted of carbon making. The lignin (Lignova™) powder and magnesium nitrate hexahydrate ($Mg(NO_3)_2 \cdot 6H_2O$; 98%, Alfa Aesar) grains were mixed, ground and homogenized with an agate mortar and pestle, followed by pyrolysis of the mixture. The lignin and $Mg(NO_3)_2 \cdot 6H_2O$ were added in a 1:2 mass ratio, respectively. The main parameters of pyrolysis were the following:

- Heating rate: 3 °C min^{-1};
- Final temperature: 800, 900, 1000 or 1100 °C, depending on the sample type;
- Residence time: 2 h;
- Cool down: natural (slow) cooling to room temperature.

The pyrolysis oven was flushed with N_2 gas for at least 15 min before each heating procedure. The material appearance obtained after the pyrolysis is a soft airy black carbon.

The next procedure involved acid washing for removal of the *in situ* formed magnesium oxide template from the carbon material. The following steps were taken:

- The pyrolyzed carbon batch was again ground with mortar and pestle
- The fine powder was then added to 1 M HCl (37%, Honeywell) solution in deionized water;
- The dispersion obtained was sonicated for at least 5 min and then mixed with a magnetic stirrer (500 rpm) for 2 h;
- Vacuum filtration and washing with Milli-Q water was performed;
- The filtrate (a black carbon powder) was dried in an oven overnight at 60 °C.

Subsequently, in the next stage, the doping of the carbon material was carried out. The steps taken in a typical synthesis were:

- The chemicals (dried carbon material, iron(II) acetate and 1,10-phenantroline) were carefully weighed using analytical balance into separate glass vials or weighing boats.
- Iron(II) acetate 5 mg mL^{-1} ethanol solution was made and sonicated for at least 15 min.
- 6.25 mg of 1,10-phenanthroline was dissolved in 1.5 ml of ethanol.
- 200 µL of iron(II) acetate solution was added to the 1,10-phenanthroline solution, and the resulting mixture solution was sonicated for at least 15 min.
- 25 mg of carbon material was then added to the mixture solution, and the dispersion obtained was sonicated for at least 30 min;
- The dispersion was dried on a petri dish in an oven at 60 °C until all the ethanol evaporated.

After the drying of carbon, flash pyrolysis is performed with the resulting material. The pyrolysis settings were the following:

- Heating rate: 50 °C min^{-1};
- Final temperature: 800 °C;
- Residence time: 1 h;
- Cool down: fast cooling (open split-type oven).

During the flash pyrolysis, the quartz tube was also flushed with N_2 gas for at least 15 min before each heating procedure. The doped carbon material (Fe-N-C catalyst) obtained again have a soft airy black carbon appearance. It is crushed with mortar and pestle to obtain a fine powder and is ready to be used in the electrochemical measurements.

3.3 Electrochemical measurements

To perform the electrochemical measurements, first it is necessary to make the catalyst suspension that will be used to coat the working electrodes. The suspension is made from the following components:

- Fe-N-C catalyst – 2 mg;
- Milli-Q water – 490 µL;
- 2-propanol (≥99.8%, Fisher) – 490 µL;
- Nafion D521 dispersion (5 wt.%, Ion Power) – 20 µL.

These components were added to a glass vial and sonicated for at least 30 minutes.

The working electrodes used were glassy carbon (GC) with a geometric surface area of 0.2 cm^2. For each set of measurements, the total volume of the catalyst suspension added to the electrodes was 20 µL. Thus, the total catalyst loading on the GC electrodes was 0.2 mg cm^{-2}. The coating solution was added with a pipette in four portions (5 µL each) with drying in an oven at 60 °C for a few min after each deposition.

The electrochemical measurements were carried out in a three-electrode setup. Cyclic voltammetry (CV) with the rotating disk electrode (RDE) as working electrode was used to measure the oxygen reduction reaction (ORR) activity of the Fe-N-C catalysts. In CV, the electrode potential is linearly ramped over time in cyclical phases. The rate of potential change during each phase is termed as the scan rate (V s^{-1}). The current is measured between the working electrode and the counter electrode. The resulting data are plotted as current density (j, mA cm^{-2}) versus potential (E, V). A computer-controlled potentiostat, connected to the three-electrode setup collected and logged the experimental data. The main data was obtained at several rotation rates of the working electrode in RDE mode.

The working electrode was the glassy carbon (GC20-SS, Tokai Carbon) with the catalyst coating as described above, the reference electrode was a saturated calomel electrode (SCE), and a Pt wire as the counter electrode. The electrolyte was a 0.1 M KOH (85%, Fisher Scientific) aqueous solution. The ORR measurements were performed in O_2 saturated solution and the background currents were recorded in an Argon saturated solution. The background currents were subtracted from the RDE polarization curves to obtain the O_2 reduction currents.

Before the main measurements were taken, the electrodes were stabilized through potential cycling. The cycling parameters were:

- Potential range: 0.0 V to -1.2 V vs. SCE;
- Scan rate: 200 mV s^{-1} in O_2 and 100 mV s^{-1} in Ar-saturated electrolyte;
- Number of scans: min. 5 cycles.

For the main measurements, the cyclic voltammetry parameters were:

- Potential range: 0 or 0.1 V to -1.2 V vs. SCE;
- Scan rate: 10 mV s^{-1};
- Electrode rotation rates: 0 (in Ar), 360, 610, 960, 1900, and 3100 rpm;
- Number of scans: 1 cycle only.

Besides the Fe-N-C catalysts, electrochemical measurements were also performed on non-doped mesoporous carbon materials (obtained after the first pyrolysis procedure) for

comparison. They were designated as C800, C900, C1000 and C1100. The numbers represent the carbonization temperature as was done with the Fe-N-C catalysts.

The accelerated stability testing of all four Fe-N-C electrocatalysts was performed by applying 15,000 potential cycles in O_2-saturated 0.1 M KOH solution in the potential range between 0 and −0.4 V vs. SCE at a scan rate of 200 mV s^{-1}. The ORR polarization curves were recorded at 1900 rpm using scan rate of 10 mV s^{-1} before and after potential cycling.

3.4 Physicochemical characterization

The following physicochemical characterization techniques were used for analyzing the catalyst materials:

- N_2 physisorption by Dr. Maike Käärik (Institute of Chemistry, University of Tartu)
- Scanning electron microscopy (SEM) with energy-dispersive X-ray analysis (EDX) by Dr. Jekaterina Kozlova (Institute of Physics, University of Tartu)
- Scanning transmission electron microscopy (STEM) by Dr. Jekaterina Kozlova (Institute of Physics, University of Tartu)
- X-ray photoelectron spectroscopy (XPS) by Dr. Arvo Kikas (Institute of Physics, University of Tartu)
- Raman spectroscopy by Dr. Aleksei Treštšalov (Institute of Physics, University of Tartu)

For SEM, XPS and Raman spectroscopy analysis, the catalyst inks were prepared via sonication − only the catalyst material under investigation, water, and isopropanol were added.

Porosity was characterized by low-temperature N_2 physisorption using a NOVAtouch LX2 analyzer (Quantachrome Instruments). Samples were degassed at 300 °C under vacuum for 12 h and backfilled with N_2. Total pore volume (V_{tot}) was calculated at $P/P_0 = 0.97$. Specific surface area (SSA_{dft}), micropore volume (V_μ) and the pore size distribution (PSD) graphs were obtained using the QSDFT model for slit/cylindrical shaped pores.

High-resolution SEM images were obtained using a Helios NanoLab 600 (FEI) at 10 kV. Elemental composition was analyzed with an INCA Energy 350 EDX spectrometer (Oxford Instruments) attached to the microscope. STEM analysis was performed at 200 kV using a Titan Themis 200 (FEI) microscope with a Cs-probe corrector. Elemental mapping was carried out via EDX using an integrated SuperX system (Bruker).

XPS analysis was performed using Mg Kα radiation (1253.6 eV) from a non-monochromatic X-ray source (Thermo XR3E2) and a SCIENTA SES 100 analyzer under ultra-high vacuum. Survey and high-resolution N 1s spectra were recorded with pass energy of 200 eV. Data were processed in CasaXPS (v2.3.17), applying satellite removal, background correction (linear/Shirley), and peak fitting with a Gauss–Lorentz (Gauss 30 %, Lorentz 70 %) function. Atomic concentrations were calculated using Scofield cross-sections and effective attenuation lengths.

Micro-Raman spectra were recorded in back-scattering geometry using an inVia Renishaw spectrometer with a 50× Olympus confocal microscope and a 514.5 nm Ar ion laser. Low laser power was used to minimize sample heating, with spectra averaged over an area of ~200 μm². A four-peak model was used for fitting: G (~1590 cm^{-1}), D1 (~1350 cm^{-1}), D3 (~1490 cm^{-1}), and D4 (~1210 cm^{-1}), corresponding to graphitic, defective, amorphous, and disordered carbon structures, respectively (Sadezky et al., 2005). D2 peak (~1614cm^{-1}) is not clearly separated as it is overlapped with G peak. Baseline correction and peak fitting were performed in OriginPro 9 using Voigt functions. Peak parameters (position, intensity, and width) were optimized by minimizing chi-square values.

4 RESULTS AND DISCUSSION

4.1 Physicochemical characterization of catalysts

Magnesium nitrate hexahydrate ($Mg(NO_3)_2 \cdot 6H_2O$) was selected as a template agent and ionic liquid for the ionothermal synthesis because it is a low-melting point salt (approximately 89°C), which is considerably below the carbonization temperature of lignin. The presence of nitrogen in the magnesium nitrate salt is particularly relevant as at the same time magnesium nitrate is an ideal ionothermal liquid reaction medium, it also introduces nitrogen moieties into the carbon matrix. During pyrolysis, lignin is partially dissolved into molten salt and the pore formation occurs through two stages. In the first stage, as the temperature increases during pyrolysis, larger pores are formed by liquid salt droplets within the carbon phase. In the next stage, as the $Mg(NO_3)_2$ decomposes, the *in situ* formed MgO nanoparticles are partially covered by the carbon phase and a composite material comprising of MgO nanoparticles and a carbon matrix is formed. The mesopores are formed after the acid-treatment procedure when the MgO nanoparticles (the sacrificial template) are washed out by dispersing the material in 1 M HCl solution (Ibrahim et al., 2025).

To study the textural properties of the prepared catalyst materials and the effect of carbonization temperature on the templating efficiency, the N_2 physisorption analysis was conducted. The results are shown in **Table 1**. For the Fe-N-C catalysts, the Fe-N-C900 material achieved the highest specific surface area (SSA) of 802 $m^2\ g^{-1}$ and the largest total pore volume (V_{tot}) of 0.85 $cm^3\ g^{-1}$. Also, the Fe-N-C1000 catalyst showed a very similar V_{tot} of 0.84 $cm^3\ g^{-1}$, together with high SSA. The Fe-N-C1100 catalyst showed significantly smaller SSA and V_{tot} than the other three synthesized Fe-N-C catalysts, which suggests that the porous structure may have partially collapsed. The average pore size (APS) increased by increasing the carbonization temperature, reaching its maximum with the Fe-N-C1100. The Fe-N-C900 and Fe-N-C1000 showed similar micro- and mesoporosity, while the Fe-N-C800 possessed higher microporosity and lower mesoporosity, and the Fe-N-C1100 material showed significantly less microporosity.

As expected, compared to C1000 material, the Fe-N-C1000 catalyst exhibited reduced SSA and V_{tot}, with larger APS, which indicates that doping caused the blocking of micropores as is also evident from reduced SSA_{μ} and V_{μ} values.

Table 1. Textural properties of MC materials: specific surface area (SSA), micro- and mesoporous SSA (SSA_{μ}, SSA_{meso}), total pore volume (V_{tot}), micro-pore volume (V_{μ}), and average pore size (APS).

Mesoporous carbon	SSA_{BET} ($m^2\ g^{-1}$)	SSA_{DFT} ($m^2\ g^{-1}$)	SSA_{μ} ($m^2\ g^{-1}$)	SSA_{meso} ($m^2\ g^{-1}$)	V_{tot} ($cm^3\ g^{-1}$)	V_{μ} ($cm^3\ g^{-1}$)	APS (nm)
Fe-N-C800	758	760	371	389	0.72	0.14	1.89
Fe-N-C900	802	790	307	483	0.85	0.11	2.15
Fe-N-C1000	729	749	301	448	0.84	0.11	2.24
Fe-N-C1100	411	375	25	350	0.60	0.02	3.20
C1000	927	941	461	480	0.93	0.17	1.98

The N_2 physisorption measurement results (**Figure 3a**) were also used to determine the pore size distributions (PSD) (**Figure 3b**), showing that for all studied materials the mesopores are mostly between 4 and 6 nm in diameter, with a peak around 5 nm. The Fe-N-C1100 material exhibited slightly less mesopores in the range between 2 and 4 nm. All materials also contain micropores, i.e. pore sizes smaller than 2 nm. However, this method is limited to 50 nm pores, thereby macropores cannot be determined. But all in all, it can be said that the templating approach taken herein has been a success as highly mesoporous Fe-N-C catalysts were obtained.

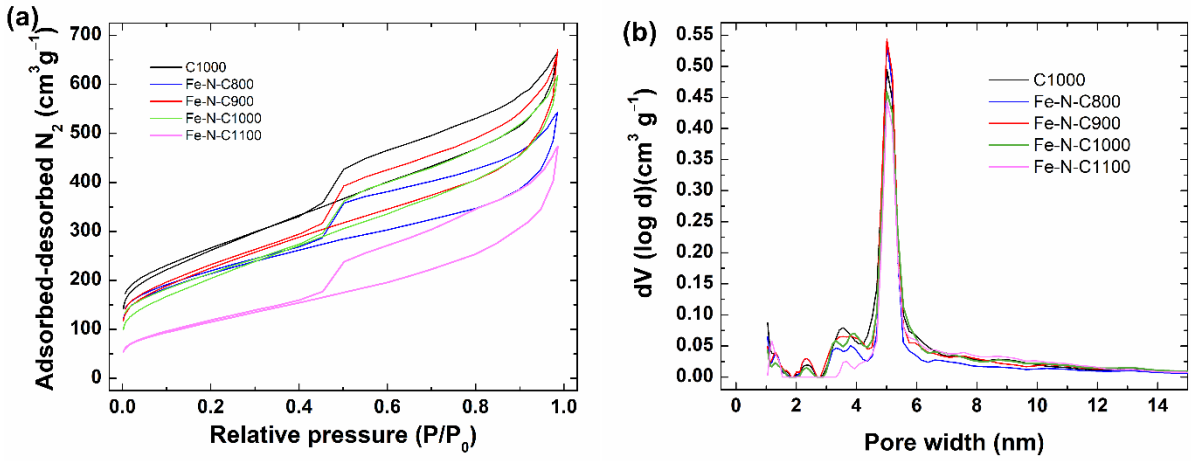

Figure 3. (a) N_2 physisorption isotherms and (b) pore size distribution (PSD) of synthesized Fe-N-C catalysts and mesoporous carbon C1000 material.

The scanning electron microscope (SEM) technique was applied on the Fe-N-C1000 sample to study its surface morphology. SEM images (**Figure 4**) reveal that a hierarchical porous material, which contains macropores and mesopores, was obtained. The higher magnification images (**Figure 4** bottom row) show that abundant small mesopores are present

in the carbon nanomaterial structure after the removal of the MgO template. The SEM-EDX analysis revealed that after the Fe,N-doping 1.3 wt.% of Fe and 3.9 wt.% of N could be detected in the Fe-N-C1000 sample. Additionally, 2.5 wt.% of Mg is left in the material, however, no indication to MgO nanoparticles were visible in the SEM images. The Mg occurring in the carbonized material could be most likely be present either as atomically dispersed atoms embedded in the carbon matrix or as MgO nanoparticles encapsulated within the carbon material that cannot be removed during acid treatment (Kisand et al., 2025).

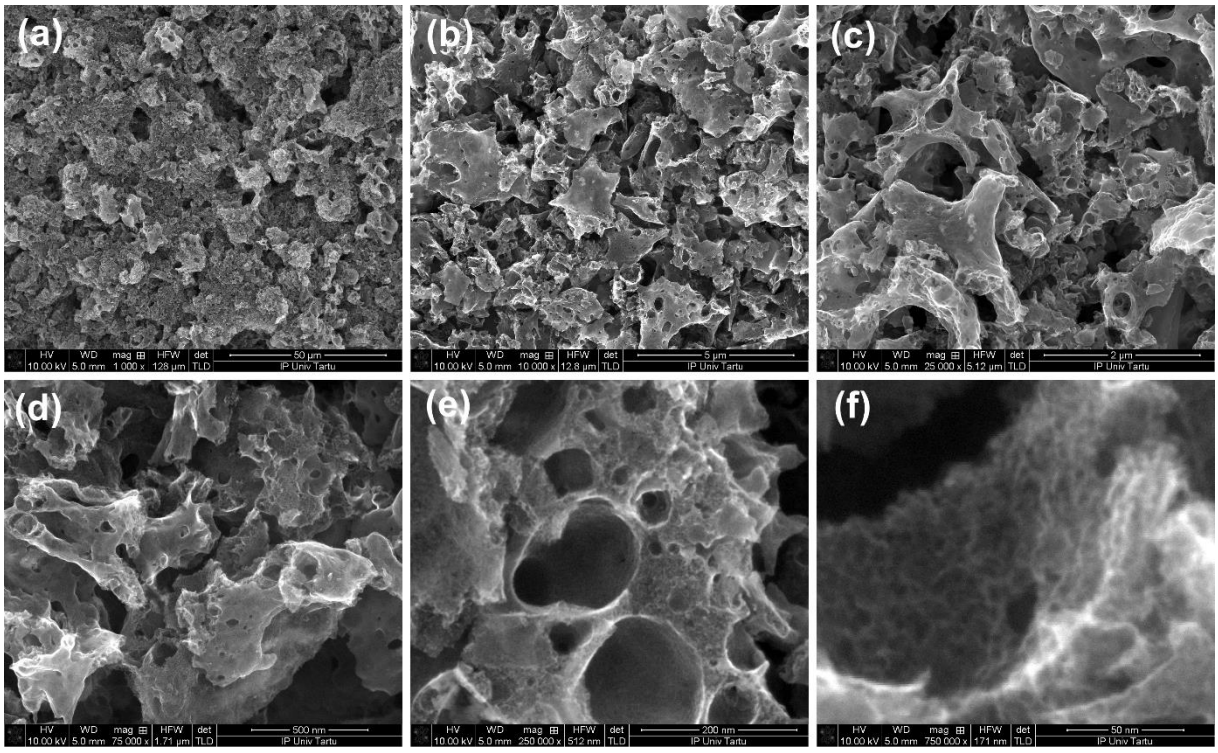

Figure 4. SEM images of Fe-N-C1000 at different magnifications.

Scanning transmission electron microscopy (STEM) was used to study the morphology of Fe-N-C1000 catalyst material further. As shown in **Figure 5a**, the STEM image reveals that the material has a hierarchical porous structure as expected. In **Figure 5b**, it is possible to observe the presence of a few metal nanoparticles within the material, however, it is not possible to assert if these are Fe nanoparticles or MgO ones. In **Figure 5c**, it is possible to see the existence of graphitic layers in the material. The high-angle annular dark field (HAADF)-STEM image (**Figure 5d**) verifies the presence of atomically dispersed metal atoms (white bright spots), presumably as Fe-N_x sites. In **Figures 5e** and **5f**, the STEM-EDX element mapping images show that a good and uniform dispersion of iron and nitrogen was achieved in the Fe-N-C1000 electrocatalyst, which indicates that the doping procedure was adequate.

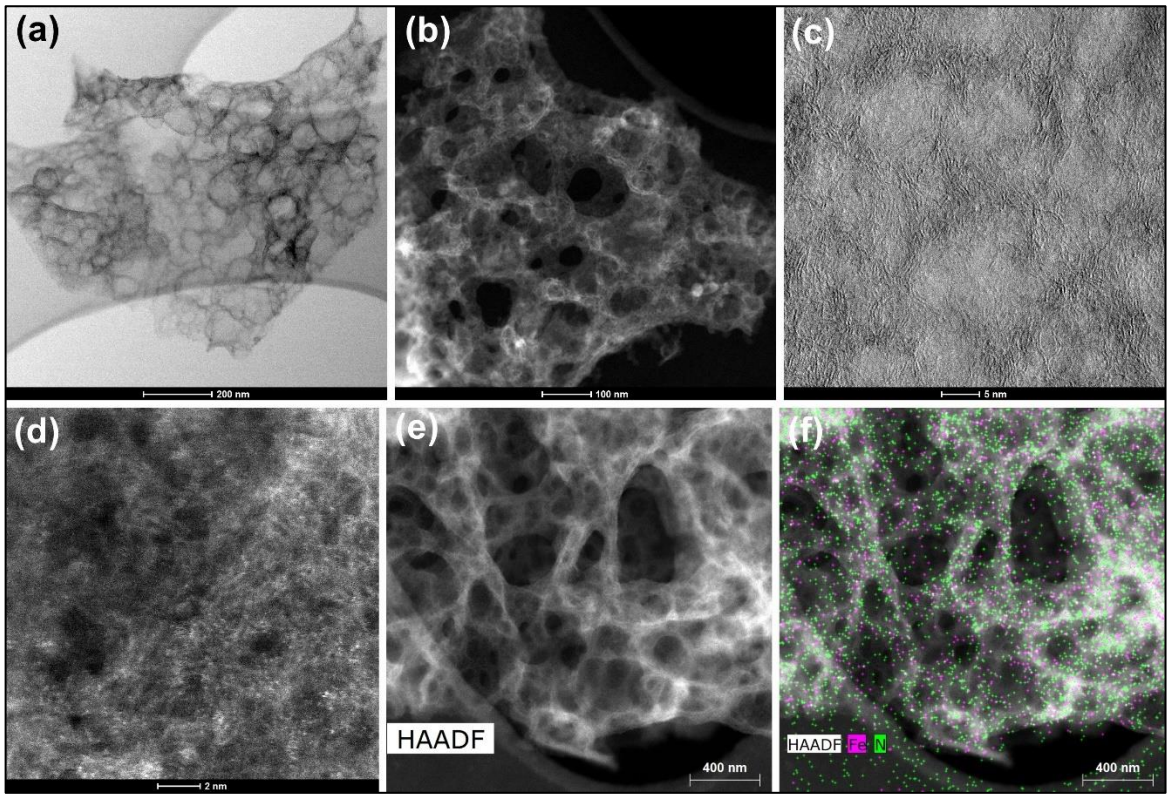

Figure 5. STEM images of the Fe-N-C1000 electrocatalyst.

Micro-Raman spectroscopy was employed to characterize all the Fe-N-C catalysts and also the non-doped C1000 material. The Raman spectra (**Figure 6a**) of all materials show two broad maxima characteristic of carbon materials: the graphitic (i.e. sp^2-hybridised) carbon (G) peak is located at approximately 1597 cm^{-1} and the disordered (e.g. vacancies, grain boundaries or sp^3-C hybridization) carbon (D) peak is located at approximately 1352 cm^{-1}.

For the evaluation of the degree of structural disorder, the widths of the D1 and G peaks at half maximum and the integrated area ratio (I_{D1}/I_{G+D2}) of the D1 and G+D2 peaks is determined. The widths of the G and the D1 band can be used for qualitative indicator of structural disorder in defective carbon materials: widths increasing with the increase in disorder in the graphitic lattice (Piir et al., 2025). All Raman spectra are rather similar and the widths of the D1 and G peaks at half maximum did not change significantly (~162 cm^{-1} for D1 band and ~93 cm^{-1} for G band) with varying the carbonization temperature nor doping. However, the I_{D1}/I_{G+D2} ratio has a clear trend to increasing with the growth of the carbonization temperature: 1.4 for Fe-N-C800, 1.4 for Fe-N-C900, 1.8 for Fe-N-C1000, 2.1 for Fe-N-C1100. The non-doped C1000 had I_{D1}/I_{G+D2} of 1.9, indicating that doping did not influence it much. At the same time, the fraction of amorphous carbon (D4 band at ~1192cm^{-1}) decreases with the growth of the carbonization temperature (example in **Figure 6b**). Higher defective samples, indicated by higher I_{D1}/I_{G+D2} ratio, are credible for having more electrocatalytically active centers, which are

beneficial to accelerate the ORR kinetics (Zhao et al., 2023). However, less amorphous carbon means that the materials carbonized at higher temperature should possess better stability (Trogadas et al., 2014).

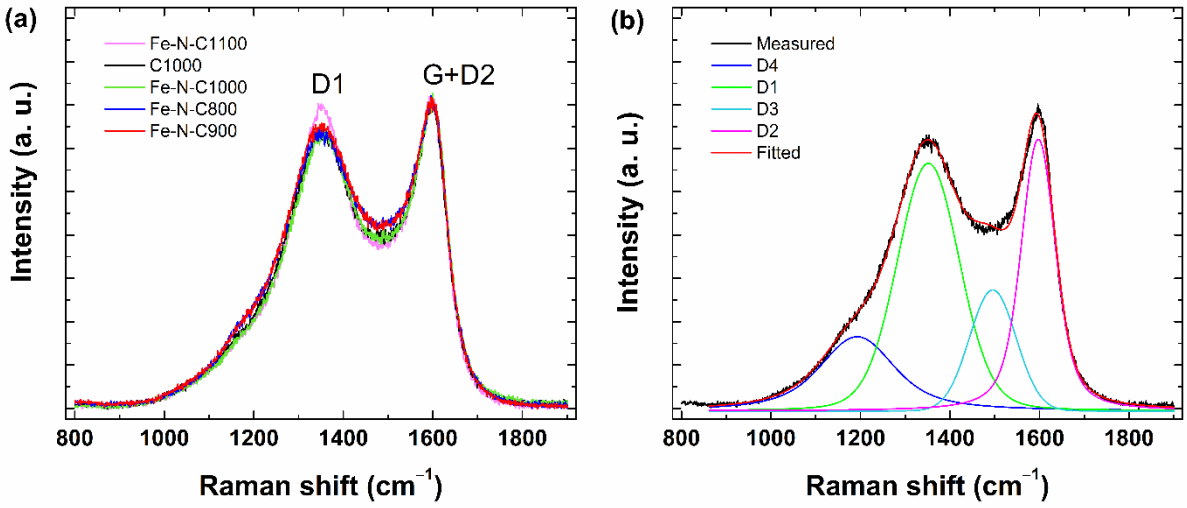

Figure 6. (a) Raman spectra of all Fe-N-C catalysts and the non-doped C1000 material. (b) Example of fitting of peaks with Fe-N-C800 sample.

The X-ray photoelectron spectroscopy (XPS) analysis was used to study the Fe-N-C catalysts surface elemental composition. The XPS spectra are shown in **Figure 7,** and the results are shown in **Table 2** and **Table 3**. The XPS analysis detected carbon, oxygen and nitrogen in all materials. All catalysts possessed surface iron content at 0.2 wt.%, except the Fe-N-C1100 sample, which did not have any iron in a detectable amount. The reason for the XPS peaks of iron to be absent is because the value of 0.2 wt.% is too low for the photoelectron peaks to clearly appear. It is possible to observe from the XPS data that there is a negative correlation between nitrogen content and pyrolysis temperature, i.e., an increase in pyrolysis temperature led to lower final nitrogen content in the catalyst materials.

The XPS analysis also allows us to distinguish and quantify different nitrogen species in the materials, which is key for identifying the nitrogen moieties that contribute to the ORR. In alkaline medium, pyridinic-N and M-N_x active sites are considered the most effective for ORR (Artyushkova et al., 2015). The XPS spectrum was analyzed more thoroughly in the N1s region and deconvoluted into seven components with example shown in **Figure 7b**. The nitrogen moieties more abundantly present in all the Fe-N-C catalyst materials were pyridinic-N and pyrrolic-N, with relative contents of ca. 30 %. Metal-N_x moieties content varied between the materials studied, with the lowest reported value of 4.6 at.% for Fe-N-C800 and the highest reported value of 18.8 at.% for the Fe-N-C900 material. The presence of multiple distinct

nitrogen moieties may be beneficial for the electrocatalytic performance of catalysts as some sites may complement each other for the complete reduction of O_2 to OH^- (Kabir et al., 2018).

Additionally, the carbon peak in the XPS spectrum was investigated more thoroughly as the C1s spectra was deconvoluted into components. In Fe-N-C materials, the relative concentrations of sp^2 and sp^3-hybridized carbon were 72-75% and 4-8%, respectively. The high sp^2-hybridized (graphitic) carbon content improves the electrical conductivity, which is essential for fast electron transfer during the ORR, and helps to maintain active site integrity by stabilizing Fe-N_x moieties (Niwa et al., 2011) (Ma et al., 2021).

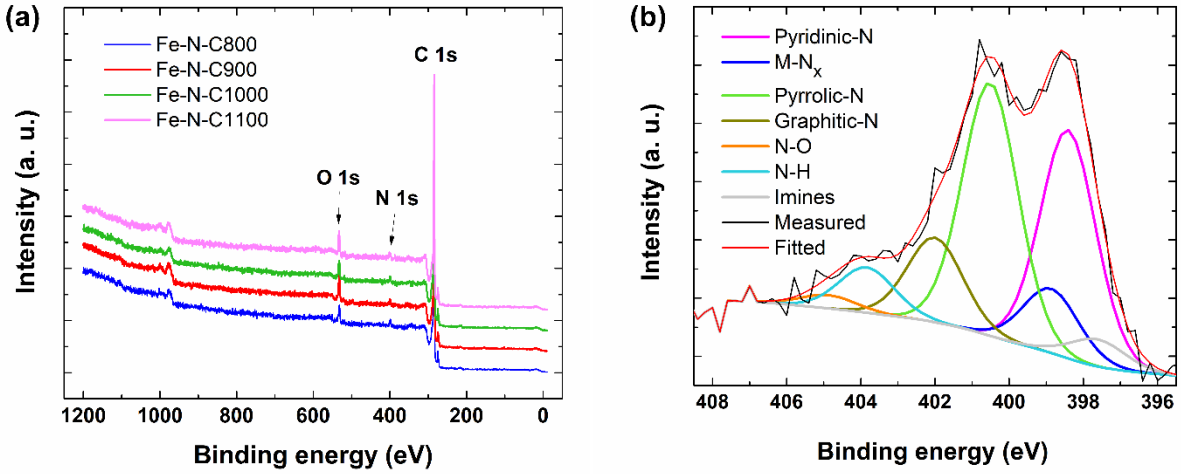

Figure 7. (a) XPS survey spectra for Fe-N-C catalyst materials and (b) XPS detailed N1s spectra for Fe-N-C1000 catalyst.

Table 2. Surface elemental composition of Fe-N-C catalyst materials as determined by XPS.

Electrocatalyst	Carbon (at.%)	Nitrogen (at.%)	Oxygen (at.%)	Iron (at.%)
Fe-N-C800	92.8	2.6	4.4	0.2
Fe-N-C900	91.1	2.4	6.4	0.2
Fe-N-C1000	93.7	2.0	4.2	0.2
Fe-N-C1100	93.1	1.7	5.2	n/d

Table 3. Relative concentration (%) of nitrogen moieties in Fe-N-C materials.

Relative content (%)	Fe-N-C800	Fe-N-C900	Fe-N-C1000	Fe-N-C1100
Imine	6.9	19.0	3.9	11.8
Pyridinic-N	35.9	20.3	31.9	29.4
Metal-N_x	4.6	18.1	8.8	8.2
Pyrrolic-N	34.7	25.3	35.3	31.2
Graphitic-N	11.2	8.9	11.8	5.3
NO	2.3	8.4	2.0	5.9
Bulk N-h	4.2	0.0	6.4	8.2
Hydrogenated N	0.0	0.0	0.0	0.0

4.2 Electrochemical characterization of catalysts

The RDE method was employed to assess the electrocatalytic oxygen reduction reaction activity of the catalyst materials prepared in this work with the respective ORR polarization curves shown in **Figure 8**.

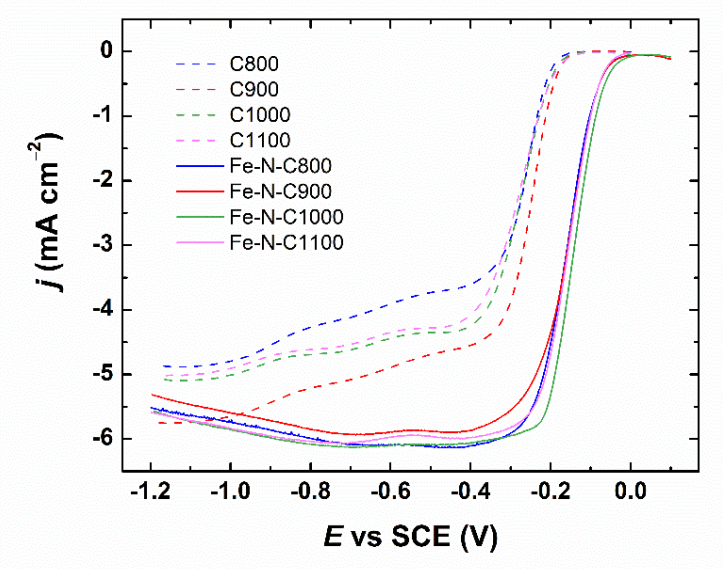

Figure 8. RDE polarization curves for oxygen reduction on Fe-N-C catalysts and non-doped carbon materials in O_2-saturated 0.1 M KOH solution at 1900 rpm.

As expected, the non-doped carbon materials showed lower electrocatalytic activity for the ORR than the Fe-N-C ones. However, their performance is better than commonly observed with pristine carbon materials, thereby indicating the presence of nitrogen-containing ORR-

active sites originating from the templating agent (Ibrahim et al., 2025). The results obtained confirm previous knowledge that pure carbonaceous materials typically have lower ORR electrocatalytic activity than carbon materials modified with non-precious metals or different heteroatoms, such as nitrogen, sulfur, phosphorus, or their combinations (Lilloja, Kibena-Põldsepp, et al., 2021).

Two important parameters for ORR measurements and comparison between different electrocatalysts are the onset potential (E_{onset}) – the potential at which the current density reaches -0.1 mA cm^{-2}, and half-wave potential ($E_{1/2}$) – the potential at which the current density is half of the value of diffusion-limited current density (j_d). The onset potentials, half-wave potentials and number of electrons transferred (n) per O_2 molecule obtained from the RDE experimental data are presented in **Table 4**. The onset potential can be understood as the potential at which the oxygen reduction wave commences. A more positive onset potential means that the electrocatalyst is more active. For Fe-N-C catalysts, the ORR onset potential is related to the Fe(III)/(II) redox transition (Zúñiga et al., 2019). The $E_{1/2}$ value shows the overall electrocatalytic activity of the catalyst, with a more positive value meaning better performance. Although the onset potential is a commonly used and generally accepted measure of electrocatalytic activity, it lacks a universally agreed definition and a standardized measurement procedure within the scientific community. Even when a specific threshold current density for ORR is applied, the reported onset potential remains sensitive to the catalyst loading and the specific surface area of the catalytic material (Batchelor-McAuley, 2023).

From **Figure 8** it is possible to observe that all Fe-N-C catalysts have similar and well-defined diffusion-limited current plateaus starting around -0.2 V vs. SCE as well as similar E_{onset} values (**Table 4**). While the non-doped carbon-based catalysts also have similar onset potentials, they have more variable and less defined diffusion-limited current plateaus. Among non-doped carbon catalysts, the one obtained with a carbonization temperature of 900 °C showed the best performance. In theory, carbon materials pyrolyzed at higher temperatures should exhibit higher degree of graphitization and improved electrical conductivity.

It can be seen from **Table 4** that the doped catalysts (Fe-N-C) possess more positive E_{onset} and $E_{1/2}$ values than non-doped materials, due to their increased ORR electrocatalytic activity. Among all the electrocatalysts studied, the Fe-N-C1000 catalyst showed the highest E_{onset} and $E_{1/2}$ values of -0.03 and -0.14 V vs. SCE, respectively. However, the other doped catalysts showed very close values, with the lowest value of -0.16 V vs. SCE reported by both Fe-N-C800 and Fe-N-C900.

Table 4. Onset potentials (E_{onset}), half-wave potentials ($E_{1/2}$) and number of electrons transferred (n) of catalyst materials in 0.1 M KOH solution.

Electrocatalyst	E_{onset} vs SCE (V)	$E_{1/2}$ vs SCE (V)	n
C800	-0.18	-0.28	2.7-3.6
C900	-0.16	-0.26	3.1-3.7
C1000	-0.17	-0.29	2.9-3.5
C1100	-0.16	-0.29	2.9-3.4
Fe-N-C800	-0.05	-0.16	3.9-4.0
Fe-N-C900	-0.04	-0.16	3.6-3.9
Fe-N-C1000	-0.03	-0.14	3.8-3.9
Fe-N-C1100	-0.04	-0.15	3.6-3.8

RDE polarization curves and K-L plots, with insets showing the number of electrons transferred per O_2 molecule as a function of potential, for the non-doped carbon material C900 and Fe-N-C1000 catalyst are shown in **Figure 9**. The K-L plots at various potentials for the Fe-N-C1000 are nearly overlapping with a y-axis intercept of the extrapolated K-L lines close to zero, which indicates that the ORR process for this catalyst material is mainly limited by the mass transfer. While the calculated n value for the Fe-N-C1000 was close to 4 in the potential range from -0.4 to -1.2 V vs. SCE, the calculated n value for the undoped C900 material was between 3.1 and 3.7 in the same range, suggesting that the 2-electron pathway, where the undesired intermediate byproduct hydroperoxide anion (HO_2^-) is formed, has a considerable contribution to the total electrochemical reduction process in the latter (Sibul et al., 2020).

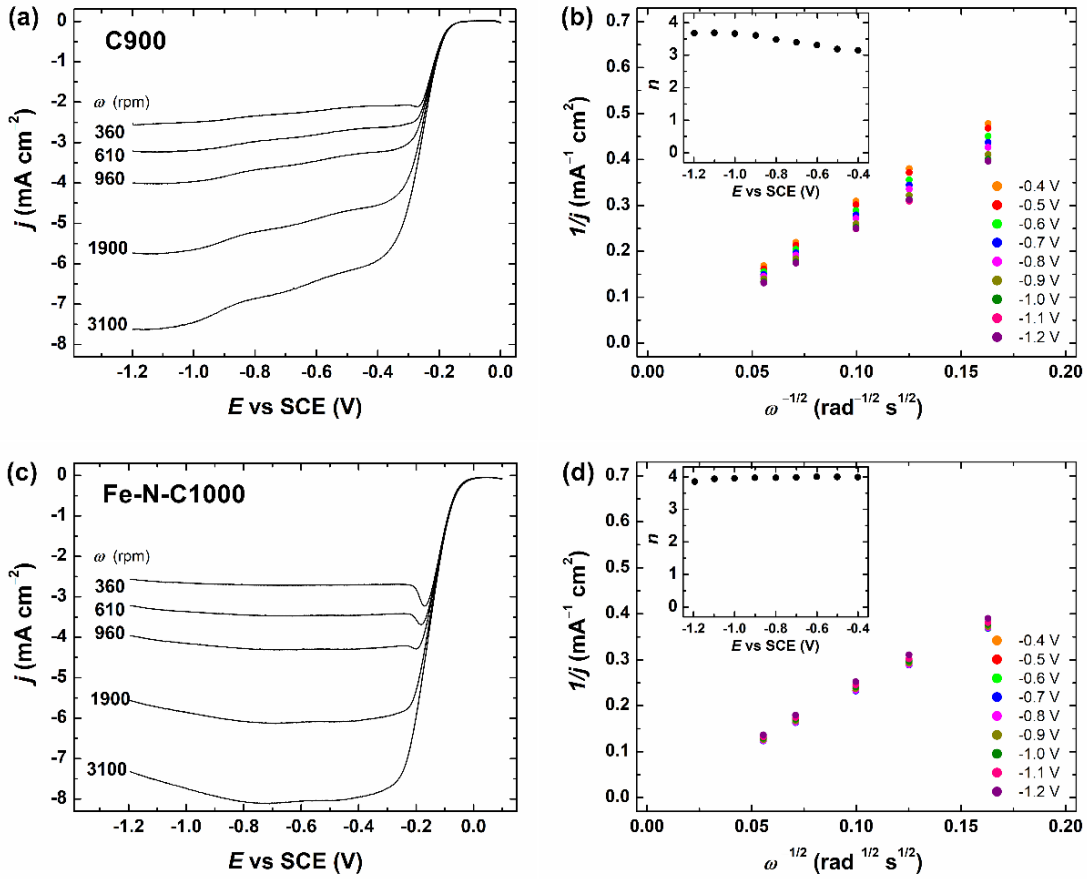

Figure 9. (a) and (c) RDE polarization curves for oxygen reduction on the non-doped carbon material C900 and Fe-N-C1000 catalyst in O_2-saturated 0.1 M KOH at various rotation rates. (b) and (d) Koutecký-Levich plots, with insets showing the number of electrons transferred per O_2 molecule as a function of potential, for the C900 and Fe-N-C1000, respectively.

Table 4 also shows that for all Fe-N-C catalysts, the *n* values are slightly below 4. This means the ORR proceeds predominantly via a 4-electron pathway or 2+2-electron pathway, where peroxide forms as an intermediate and is then mostly further reduced to OH^- anions. An *n* value equal to 4 indicates that the catalysts promote the complete reduction of O_2 to OH^-, which is the preferred pathway for ORR in fuel cells. The 4-electron pathway maximizes energy output in fuel cells and eliminates the production of unwanted byproducts such as peroxides, which can possibly degrade the catalyst materials and ion exchange membranes (Hossen et al., 2023). For the non-doped carbon catalysts, a lower *n* value is found. This means that typically only 2-electron ORR pathway occurs, or less peroxide ions are being reduced further to OH^-. It is also possible to see from **Table 4** that the catalysts of the same type, non-doped or doped ones, show similar results. Considering some experimental error must have been present, it is likely that the carbonization temperature did not significantly affect the main ORR parameters of the catalysts synthesised in this work.

The results of the short-term electrochemical stability tests (**Figure 10**) performed with Fe-N-C catalysts show that, for all of them, no substantial decrease in the ORR activity after 15,000 potential cycles was observed, with only a slight decrease in the ORR onset potential, half-wave potential, and diffusion-limited current density values. No E_{onset} and $E_{1/2}$ shifts larger than 5 mV after 15,000 cycles was observed. It is also possible to notice a slight positive tendency for the catalysts to become more stable with increasing carbonization temperature, with the Fe-N-C1100 material possessing the smallest E_{onset} and $E_{1/2}$ drops and the smallest decrease of diffusion-limited current density values among them all. The j_d values after stability testing could indicate slightly lower *n*. value, suggesting that higher carbonization temperature improves the stability of active sites that facilitate 4-electron ORR process.

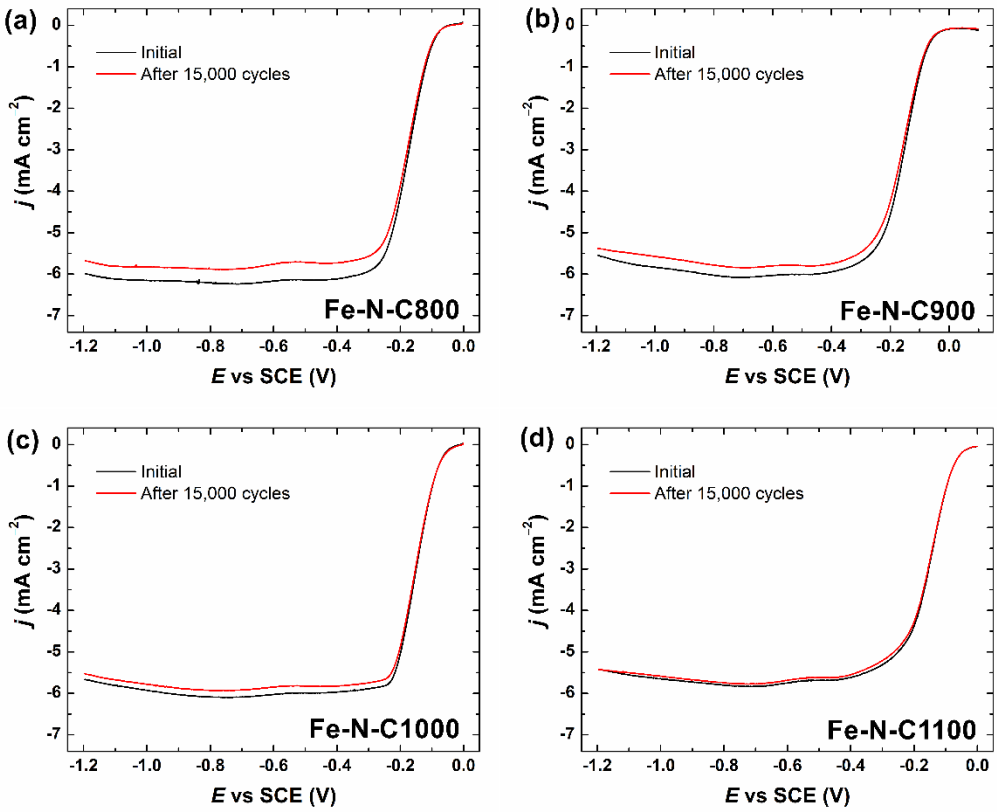

Figure 10. RDE voltammetry curves for oxygen reduction on Fe-N-C catalysts in O_2-saturated 0.1 M KOH solution before and after applying 15,000 potential cycles.

SUMMARY

This thesis aimed to develop non-precious metal Fe-N-C electrocatalysts that have the potential to replace expensive PGM-based catalysts, such as carbon-supported platinum nanoparticles (Pt/C), currently used for the oxygen reduction reaction (ORR) in an anion-exchange membrane fuel cell (AEMFC) cathodes. The hierarchical porous carbon materials were synthesized via templating-method using ionothermal synthesis and high-temperature pyrolysis with lignin as sustainable carbon precursor. Iron and nitrogen doping was carried out by flash pyrolysis using iron(II) acetate and 1,10-phenanthroline as precursors. Electrochemical characterization of catalyst materials was performed using the three-electrode setup and rotating disk electrode (RDE) method in 0.1 M KOH solution. Several analytical methods were utilized for physicochemical characterization of the catalyst materials: scanning electron microscopy (SEM), scanning transmission electron microscopy (STEM), N_2 physisorption, X-ray photoelectron spectroscopy (XPS), and Raman spectroscopy.

The electrochemical results reveal that all synthesized Fe-N-C catalysts show outstanding ORR electrocatalytic activity in alkaline solution. The Fe-N-C1000 material, based on lignin-derived carbon obtained at the carbonization temperature of 1000 °C, exhibited the best ORR performance than the catalyst material obtained at other temperatures by achieving half-wave potential of −0.14 V vs SCE. The Koutecký-Levich analysis shows that the Fe-N-C materials favor 4-electron or 2+2-electron ORR pathways, where O_2 is almost completely reduced to OH^- ions that is most desirable for AEMFCs. The short-term stability testing showed that the ORR activity of all Fe-N-C materials remained virtually the same after applying 15,000 potential cycles with slight positive correlations observed with the increasing carbonization temperature.

The physicochemical characterization showed the Fe-N-C materials synthesized are indeed hierarchical porous carbons with high specific surface are (up to 802 $m^2\ g^{-1}$), ideal for fuel cell electrocatalysts, containing abundant mesopores with mostly 4 and 6 nm in diameter. The success of doping was proven by SEM and XPS analysis with the materials containing ca. 1.3 wt.% of Fe and 3.9 wt.% of N. STEM analysis reveals a uniform dispersion of iron and nitrogen in the material after doping with iron being atomically dispersed. Both Raman and XPS analysis revealed that these lignin-based Fe-N-C electrocatalysts have high graphitization level with ratio of amorphous carbon reducing with increasing of carbonization temperature.

The Fe-N-C1000 electrocatalyst showed the best electrocatalytic ORR activity with suitable physicochemical properties. Further studies need to be executed to investigate the electrocatalytic performance of the Fe-N-C1000 in a fuel cell environment (AEMFC testing).

REFERENCES

Adabi, H., Santori, P., Shakouri, A., Peng, X., Yassin, K., Rasin, I., Brandon, S., Dekel, D. R., Ul Hassan, N., Sougrati, M.-T., Zitolo, A., Varcoe, J. R., Regalbuto, J. R., Jaouen, F. & Mustain, W. E. (2021). Understanding how single-atom site density drives the performance and durability of PGM-free Fe-N-C cathodes in anion exchange membrane fuel cells. *Materials Today Advances*, *12*, Article 100179. https://doi.org/10.1016/j.mtadv.2021.100179

Adabi, H., Shakouri, A., Ul Hassan, N., Varcoe, J., Zulevi, B., Serov, A., Regalbuto, J. R. & Mustain, W. E. (2021). High-performing commercial Fe-N-C cathode electrocatalyst for anion-exchange membrane fuel cells. *Nature Energy*, *6*, 834-843. https://doi.org/10.1038/s41560-021-00878-7

Adabi, H., Shakouri, A., Zitolo, A., Asset, T., Khan, A., Bohannon, J., Chattot, R., Williams, C., Jaouen, F., Regalbuto, J. R. & Musstain, W. E. (2023). Multi-atom Pt and PtRu catalysts for high performance AEMFCs with ultra-low PGM content. *Applied Catalysis B-Environment and Energy*, *325*, Article 122375. https://doi.org/10.1016/j.apcatb.2023.122375

Ahmed, Z., Akula, S., Kozlova, J., Piirsoo, H., Kukli, K., Kikas, A., Kisand, V., Käärik, M., Leis, J., Treshchalov, A., Aruväli, J. & Tammeveski, K. (2024). Hybrid high-performance oxygen reduction reaction Fe-N-C electrocatalyst for anion exchange membrane fuel cells. *International Journal of Hydrogen Energy*, *62*, 849-858. https://doi.org/10.1016/j.ijhydene.2024.03.055

Artyushkova, K., Rojas-Carbonell, S., Santoro, C., Weiler, E., Serov, A., Awais, R., Gokhale, R. R. & Atanassov, P. (2019). Correlations between Synthesis and Performance of Fe-Based PGM-Free Catalysts in Acidic and Alkaline Media: Evolution of Surface Chemistry and Morphology. *ACS Applied Energy Materials*, *2*, 5406-5418. https://doi.org/10.1021/acsaem.9b00331

Artyushkova, K., Serov, A., Rojas-Carbonell, S., & Atanassov, P. (2015). Chemistry of Multitudinous Active Sites for Oxygen Reduction Reaction in Transition Metal-Nitrogen-Carbon Electrocatalysts. *Journal of Physical Chemistry C*, *119*, 25917-25928. https://doi.org/10.1021/acs.jpcc.5b07653

Bard, A. J. & Faulkner, L. R. (2001). *Electrochemical Methods: Fundamentals and Applications*, 2nd ed., John Wiley & Sons, New York.

Batchelor-McAuley, C. (2023). Defining the onset potential. *Current Opinion in Electrochemistry*, *37*, Article 101176. https://doi.org/10.1016/j.coelec.2022.101176

Braga, L., Silveira, J., da Silva, M., Machin, E., Pedroso, D., & Tuna, C. (2014). Comparative analysis between a PEM fuel cell and an internal combustion engine driving an electricity generator: Technical, economical and ecological aspects. *Applied Thermal Engineering*, *63*, 354-361. https://doi.org/10.1016/j.applthermaleng.2013.10.053

Cai, N., Fu, L., Yang, Z., & Huang, D. (2022). Innovative strategies to effectively increase the active- site density of M-N-C materials for electrochemical application. *Current Opinion in Electrochemistry*, *34*, Article 100994. https://doi.org/10.1016/j.coelec.2022.100994

Cao, H., Pan, J., Zhu, H., Sun, Z., Wang, B., Zhao, J., & Yan, F. (2021). Interaction Regulation Between Ionomer Binder and Catalyst: Active Triple-Phase Boundary and High Performance Catalyst Layer for Anion Exchange Membrane Fuel Cells. *Advanced Science*, *8*, Article 2101744. https://doi.org/10.1002/advs.202101744

Chae, J., Choi, J., Lee, S., Park, C., & Kim, S. (2024). Effects of fabrication parameters of membrane-electrode assembly for high-performance anion exchange membrane fuel cells. *Journal of Industrial and Engineering Chemistry*, *133*, 255-262. https://doi.org/10.1016/j.jiec.2023.11.063

Chen, Z., Higgins, D., Yu, A., Zhang, L., & Zhang, J. (2011). A review on non-precious metal electrocatalysts for PEM fuel cells. *Energy & Environmental Science*, *4*, 3167-3192. https://doi.org/10.1039/c0ee00558d

Collins, G., Kasturi, P., Karthik, R., Shim, J., Sukanya, R., & Breslin, C. (2023). Mesoporous carbon-based materials and their applications as non-precious metal electrocatalysts in the oxygen reduction reaction. *Electrochimica Acta*, *439*, Article 141678. https://doi.org/10.1016/j.electacta.2022.141678

Das, G., Choi, J., Nguyen, P., Kim, D., & Yoon, Y. (2022). Anion Exchange Membranes for Fuel Cell Application: A Review. *Polymers*, *14*, Article 1197. https://doi.org/10.3390/polym14061197

Dekel, D. (2018). Review of cell performance in anion exchange membrane fuel cells. *Journal of Power Sources*, *375*, 158-169. https://doi.org/10.1016/j.jpowsour.2017.07.117

Firouzjaie, H., & Mustain, W. (2020). Catalytic Advantages, Challenges, and Priorities in Alkaline Membrane Fuel Cells. *ACS Catalysis*, *10*, 225-234. https://doi.org/10.1021/acscatal.9b03892

Fu, R., Li, Z., Liang, Y., Li, F., Xu, F., & Wu, D. (2011). Hierarchical porous carbons: design, preparation, and performance in energy storage. *New Carbon Materials*, *26*, 171-178. https://doi.org/10.1016/S1872-5805(11)60074-7

Fu, Z., Lu, L., Zhang, C., Xu, Q., Zhang, X., Gao, Z., & Li, J. (2023). Fuel cell and hydrogen in maritime application: A review on aspects of technology, cost and regulations. *Sustainable Energy Technologies and Assessments*, *57*, Article 103181. https://doi.org/10.1016/j.seta.2023.103181

Gottesfeld, S., Dekel, D., Page, M., Bae, C., Yan, Y., Zelenay, P., & Kim, Y. (2018). Anion exchange membrane fuel cells: Current status and remaining challenges. *Journal of Power Sources*, *375*, 170-184. https://doi.org/10.1016/j.jpowsour.2017.08.010

Hossen, M., Hasan, S., Sardar, R., Haider, J., Mottakin, Tammeveski, K., & Atanassov, P. (2023). State-of-the-art and developmental trends in platinum group metal-free cathode catalyst for anion exchange membrane fuel cell (AEMFC). *Applied Catalysis B-Environment and Energy*, *325*, Article 121733. https://doi.org/10.1016/j.apcatb.2022.121733

Hren, M., Bozic, M., Fakin, D., Kleinschek, K., & Gorgieva, S. (2021). Alkaline membrane fuel cells: anion exchange membranes and fuels. *Sustainable Energy & Fuels*, *5*, 604-637. https://doi.org/10.1039/d0se01373k

Ibrahim, F. O., Kisand, K., Douglin, J. D., Sarapuu, A., Kikas, A., Käärik, M., Kozlova, J., Aruväli, J., Treshchalov, A., Leis, J., Kisand, V., Kukli, K., Yassin, K., Dekel, D. R. & Tammeveski, K. (2025). Ionothermal synthesis of mesoporous FeNC electrocatalysts for high-performance anion-exchange membrane fuel cells. *Chemical Engineering Journal*, *510*, Article 161560. https://doi.org/10.1016/j.cej.2025.161560

Inagaki, M., Toyoda, M., Soneda, Y., & Morishita, T. (2018). Nitrogen-doped carbon materials. *Carbon*, *132*, 104-140. https://doi.org/10.1016/j.carbon.2018.02.024

Kabir, S., Artyushkova, K., Serov, A., & Atanassov, P. (2018). Role of Nitrogen Moieties in N-Doped 3D-Graphene Nanosheets for Oxygen Electroreduction in Acidic and Alkaline

Media. *ACS Applied Materials & Interfaces*, *10*, 11623-11632. https://doi.org/10.1021/acsami.7b18651

Kisand, K., Sarapuu, A., Douglin, J., Kikas, A., Käärik, M., Kozlova, J., Aruväli, J., Treshchalov, A., Leis, J., Kisand, V., Kukli, K., Dekel, D. R., & Tammeveski, K. (2025). Hierarchically Porous Fe-N-C Single-Atom Catalysts via Ionothermal Synthesis for Oxygen Reduction Reaction. *ChemSusChem*, *18*, Article e202401332. https://doi.org/10.1002/cssc.202401332

Lilloja, J., Fetuga, O. E. , Kibena-Põldsepp, E., Kikas, A., Käärik, M., Aruväli, J., Kozlova, J., Treshchalov, A., Kisand, V., Leis, J., Kukli, K., & Tammeveski, K. (2024). Iron- and Nitrogen-Containing Carbon Nanotube/Carbide-Derived Carbon-Based Electrocatalysts for Oxygen Reduction Reaction in Acidic Conditions. *ChemElectroChem*, *11,* Article e202400341. https://doi.org/10.1002/celc.202400341

Lilloja, J., Kibena-Põldsepp, E., Sarapuu, A., Douglin, J., Käärik, M., Kozlova, J., Paiste, P., Kikas, A., Aruväli, J., Leis, J., Sammelselg, V., Dekel, D. R., & Tammeveski, K. (2021). Transition-Metal- and Nitrogen-Doped Carbide-Derived Carbon/Carbon Nanotube Composites as Cathode Catalysts for Anion-Exchange Membrane Fuel Cells. *ACS Catalysis*, *11*, 1920-1931. https://doi.org/10.1021/acscatal.0c03511

Lilloja, J., Mooste, M., Kibena-Põldsepp, E., Sarapuu, A., Zulevi, B., Kikas, A., Piirsoo, H.-M., Tamm, A., Kisand, A., Holdcroft, S., Serov, A., & Tammeveski, K. (2021). Mesoporous iron-nitrogen co-doped carbon material as cathode catalyst for the anion exchange membrane fuel cell. *Journal of Power Sources Advances*, *8*, Article 100052. https://doi.org/10.1016/j.powera.2021.100052

Lu, X., Yang, P., Wan, Y., Zhang, H., Xu, H., Xiao, L., Li, R., Li, Y., Zhang, J., & An, M. (2023). Active site engineering toward atomically dispersed M-N-C catalysts for oxygen reduction reaction. *Coordination Chemistry Reviews*, *495*, Article 215400. https://doi.org/10.1016/j.ccr.2023.215400

Ma, Q., Jin, H., Zhu, J., Li, Z., Xu, H., Liu, B., Zhang, Z., Ma, J., & Mu, S. (2021). Stabilizing Fe-N-C Catalysts as Model for Oxygen Reduction Reaction. *Advanced Science*, *8*, Article 2102209. https://doi.org/10.1002/advs.202102209

Mehdipour-Ataei, S., & Aram, E. (2023). Mesoporous Carbon-Based Materials: A Review of Synthesis, Modification, and Applications. *Catalysts*, *13*, Article 2. https://doi.org/10.3390/catal13010002

Miyazaki, K. (2014). Electrocatalysts and Triple-Phase Boundary for Anion-Exchange Membrane Fuel Cells. *Electrochemistry*, *82*, 730-735. https://doi.org/10.5796/electrochemistry.82.730

Nazir, H., Muthuswamy, N., Louis, C., Jose, S., Prakash, J., Buan, M., Flox, C., Chavan, S., Shi, X., Kauranen, P., Kallio, T., Maia, G., Tammeveski, K., Lymperopoulos, N., Carcadea, E., Veziroglu, E., Iranzo, A. & Kannan, A. M. (2020). Is the H_2 economy realizable in the foreseeable future? Part III: H_2 usage technologies, applications, and challenges and opportunities. *International Journal of Hydrogen Energy*, *45*, 28217-28239. https://doi.org/10.1016/j.ijhydene.2020.07.256

Niwa, H., Kobayashi, M., Horiba, K., Harada, Y., Oshima, M., Terakura, K., Ikeda, T., Koshigoe, Y., Ozaki, J., Miyata, S., Ueda, S., Yamashita, Y., Yoshikawa, H., & Kobayashi, K. (2011). X-ray photoemission spectroscopy analysis of N-containing carbon-based cathode catalysts for polymer electrolyte fuel cells. *Journal of Power Sources*, *196*, 1006-1011. https://doi.org/10.1016/j.jpowsour.2010.08.054

Piir, J., Lilloja, J., Käärik, M., Kozlova, J., Kikas, A., Treshchalov, A., Aruväli, J., Kisand, V., Leis, J., Kukli, K., & Tammeveski, K. (2025). Mesoporous carbon materials doped with Co, Fe and nitrogen as oxygen reduction reaction electrocatalysts for anion-exchange membrane fuel cell. *Electrochimica Acta*, *527*, Article 146226. https://doi.org/10.1016/j.electacta.2025.146226

Rahman, M., Ara, M., Alim, M., Uddin, M., Najda, A., Albadrani, G., Sayed, A. A., Mousa, S. A., & Abdel-Daim, M. M. (2021). Mesoporous Carbon: A Versatile Material for Scientific Applications. *International Journal of Molecular Sciences*, *22*, Article 4498. https://doi.org/10.3390/ijms22094498

Rouquerol, J., Avnir, D., Fairbridge, C., Everett, D., Haynes, J., Pernicone, N., Ramsay, J. D. F., Sing, K. S. W., & Unger, K. K. (1994). Recommendations for the characterization of porous solids. *Pure And Applied Chemistry*, *66*, 1739-1758.

Sadezky, A., Muckenhuber, H., Grothe, H., Niessner, R., & Pöschl, U. (2005). Raman micro spectroscopy of soot and related carbonaceous materials:: Spectral analysis and structural information. *Carbon*, *43*, 1731-1742. https://doi.org/10.1016/j.carbon.2005.02.018

Sajjad, U., Sarapuu, A., Douglin, J. C., Kikas, A., Treshchalov, A., Käärik, M., Kozlova, J., Aruväli, J., Leis, J., Kisand, V., Kukli, K., Dekel, D. R., & Tammeveski, K. (2024). Lignin-Derived Precious Metal-Free Electrocatalysts for Anion-Exchange Membrane Fuel Cell Application. *ACS Catalysis, 14,* 9224–9234. https://doi.org/10.1021/acscatal.4c02136

Sarapuu, A., Lilloja, J., Akula, S., Zagal, J., Specchia, S., & Tammeveski, K. (2023). Recent Advances in Non-Precious Metal Single-Atom Electrocatalysts for Oxygen Reduction Reaction in Low-Temperature Polymer-Electrolyte Fuel Cells. *ChemCatChem*, *15,* Aricle e202300849. https://doi.org/10.1002/cctc.202300849

Serov, A., Shum, A., Xiao, X., De Andrade, V., Artyushkova, K., Zenyuk, I., & Atanassov, P. (2018). Nano-structured platinum group metal-free catalysts and their integration in fuel cell electrode architectures. *Applied Catalysis B-Environmental*, *237*, 1139-1147. https://doi.org/10.1016/j.apcatb.2017.08.067

Sibul, R., Kibena-Põldsepp, E., Ratso, S., Kook, M., Sougrati, M., Käärik, M., Merisalu, M., Aruväli, J., Paiste, P., Treshchalov, A., Leis, J., Kisand, V., Sammelselg, V., Holdcroft, S., Jaouen, F., & Tammeveski, K. (2020). Iron- and Nitrogen-Doped Graphene-Based Catalysts for Fuel Cell Applications. *ChemElectroChem*, *7*, 1739-1747. https://doi.org/10.1002/celc.202000011

Sljukic, B., Banks, C., & Compton, R. (2005). An overview of the electrochemical reduction of oxygen at carbon-based modified electrodes. *Journal of The Iranian Chemical Society*, *2*, 1-25.

Teppor, P., Jäger, R., Koppel, M., Volobujeva, O., Palm, R., Månsson, M., Härk, E., Kochovski, Z., Aruväli, J., Kooser, K., Granroth, S., Käämbre, T., Nerut, J., & Lust, E. (2024). Unlocking the porosity of Fe-N-C catalysts using hydroxyapatite as a hard template en route to eco-friendly high-performance AEMFCs. *Journal of Power Sources*, *591*, Article 233816. https://doi.org/10.1016/j.jpowsour.2023.233816

Trogadas, P., Fuller, T., & Strasser, P. (2014). Carbon as catalyst and support for electrochemical energy conversion. *Carbon*, *75*, 5-42. https://doi.org/10.1016/j.carbon.2014.04.005

Turtayeva, Z., Xu, F., Dillet, J., Mozet, K., Peignier, R., Celzard, A., & Maranzana, G. (2024). Investigation of membranes-electrodes assemblies in anion exchange membrane fuel

cells (AEMFCs): Influence of ionomer ratio in catalyst layers. *Heliyon*, *10*, Article e29622. https://doi.org/10.1016/j.heliyon.2024.e29622

Wang, D., Yang, P., Liu, L., Wang, W., & Chen, Z. (2022). Atomically dispersed metal-nitrogen-carbon electrocatalysts for oxygen reduction reaction: from synthesis strategies to activity engineering. *Materials Today Energy*, *26*, Article 101017. https://doi.org/10.1016/j.mtener.2022.101017

Wang, Q., Guesmi, H., Tingry, S., Cornu, D., Holade, Y., & Minteer, S. (2022). Unveiling the Pitfalls of Comparing Oxygen Reduction Reaction Kinetic Data for Pd-Based Electrocatalysts without the Experimental Conditions of the Current-Potential Curves. *ACS Energy Letters*, *7*, 952-957. https://doi.org/10.1021/acsenergylett.2c00181

Wang, Y., Chen, K., Mishler, J., Cho, S., & Adroher, X. (2011). A review of polymer electrolyte membrane fuel cells: Technology, applications, and needs on fundamental research. *Applied Energy*, *88*, 981-1007. https://doi.org/10.1016/j.apenergy.2010.09.030

Xu, H., Li, H., Xie, L., Zhao, D., & Kong, B. (2022). Interfacial Assembly of Functional Mesoporous Carbon-Based Materials into Films for Batteries and Electrocatalysis. *Advanced Materials Interfaces*, *9*, Article 2101998. https://doi.org/10.1002/admi.202101998

Xu, S., Kim, Y., Higgins, D., Yusuf, M., Jaramillo, T., & Prinz, F. (2017). Building upon the Koutecky-Levich Equation for Evaluation of Next-Generation Oxygen Reduction Reaction Catalysts. *Electrochimica Acta*, *255*, 99-108. https://doi.org/10.1016/j.electacta.2017.09.145

Zhang, B., Guo, H., Zhang, L., Zhang, X., Zhang, C., & Liu, T. (2022). Carbon composites from iron-chelating pyridine nitrogen-rich coordinated nanosheets for oxygen reduction. *Functional Composite Materials*, *3*, 2.

Zhang, J., Zhu, W., Huang, T., Zheng, C., Pei, Y., Shen, G., Nie, Z., Xiao, D., Yin, Y., & Guiver, M. (2021). Recent Insights on Catalyst Layers for Anion Exchange Membrane Fuel Cells. *Advanced Science*, *8*, Article 2100284. https://doi.org/10.1002/advs.202100284

Zhao, Z., Chen, H., Zhang, W., Yi, S., Chen, H., Su, Z., Niu, B., Zhang, Y., & Long, D. (2023). Defect engineering in carbon materials for electrochemical energy storage and catalytic conversion. *Materials Advances*, *4*, 835-867. https://doi.org/10.1039/d2ma01009g

Zhou, W., Zhi, Y., & Wang, J. (2025). Mesoporous carbon materials: synthesis methods, properties, and advanced applications. *Frontiers in Materials*, *12*, Article 1548671. https://doi.org/10.3389/fmats.2025.1548671

Zúñiga, C., Candia-Onfray, C., Venegas, R., Muñoz, K., Urra, J., Sánchez-Arenillas, M., Marco, J. F., Zagal, J. H., & Recio, F. (2019). Elucidating the mechanism of the oxygen reduction reaction for pyrolyzed Fe-N-C catalysts in basic media. *Electrochemistry Communications*, *102*, 78-82. https://doi.org/10.1016/j.elecom.2019.04.005

NON-EXCLUSIVE LICENCE TO REPRODUCE THESIS AND MAKE THESIS PUBLIC

I, Vitor Meira Chaves Barbalho,

1. grant the University of Tartu a free permit (non-exclusive licence) to reproduce, for the purpose of preservation, including for adding to the digital archives of the University of Tartu until the expiry of the term of copyright, my thesis “Iron and nitrogen doped hierarchical porous lignin-derived carbons as oxygen reduction reaction electrocatalysts”, supervised by PhD Jaana Lilloja and Prof. Kaido Tammeveski
2. grant the University of Tartu the permit to make the thesis specified in point 1 available to the public via the web environment of the University of Tartu, including via the digital archives, under the Creative Commons licence CC BY NC ND 4.0, which allows, by giving appropriate credit to the author, to reproduce, distribute the work and communicate it to the public, and prohibits the creation of derivative works and any commercial use of the work from **20/05/2026** until the expiry of the term of copyright;
3. am aware that the author retains the rights specified in points 1 and 2;
4. confirm that granting the non-exclusive licence does not infringe other persons’ intellectual property rights or rights arising from the personal data protection legislation.

Vitor Meira Chaves Barbalho

20/05/2025